

Surface brightness discontinuities in radio halos

Insights from the MeerKAT Galaxy Cluster Legacy Survey

Andrea Botteon¹, Maxim Markevitch², Reinout J. van Weeren³, Gianfranco Brunetti¹, and Timothy W. Shimwell^{4,3}

¹ INAF - IRA, via P. Gobetti 101, I-40129 Bologna, Italy
e-mail: andrea.botteon@inaf.it

² NASA/Goddard Space Flight Center, Greenbelt, MD 20771, USA

³ Leiden Observatory, Leiden University, PO Box 9513, NL-2300 RA Leiden, The Netherlands

⁴ ASTRON, the Netherlands Institute for Radio Astronomy, Postbus 2, NL-7990 AA Dwingeloo, The Netherlands

Received XXX; accepted YYY

ABSTRACT

Context. Dynamical motions in the intra-cluster medium (ICM) can imprint distinctive features on X-ray images that map the thermal bremsstrahlung emission from galaxy clusters, such as sharp surface brightness discontinuities due to shocks and cold fronts. The gas dynamics during cluster mergers may also drive large-scale turbulence in the ICM, which in turn generates extended (megaparsec-scale) synchrotron sources known as radio halos.

Aims. Surface brightness edges have been found numerous times in the thermal gas of clusters based on X-ray observations. In contrast, edges in radio halos have only been observed in a handful of cases. Our goal is to search for new radio surface brightness discontinuities in the ICM.

Methods. We inspected the images of the Bullet Cluster and the other 25 radio halos reported in the MeerKAT Galaxy Cluster Legacy Survey. To aid the identification of surface brightness discontinuities, we applied a gradient-filtering edge-detection method to the radio images.

Results. We find that the adopted filtering technique is helpful in identifying surface brightness edges in radio images, allowing us to identify at least one gradient in half of the radio halos studied. For the Bullet Cluster, we find excellent agreement between the locations of the four radio discontinuities detected and the X-ray edges. This similarity informs us that there is substantial interplay between thermal and nonthermal components in galaxy clusters. This interplay is likely due to the frozen-in ICM magnetic field, which mediates the advection of cosmic rays while being dragged by thermal gas flows.

Conclusions. We conclude that radio halos are shaped by dynamical motions in the ICM and that they often display surface brightness discontinuities, which appear to be co-located with edges in the thermal gas emission. Our results demonstrate that new and future generations of radio telescopes will provide an approach to efficiently detecting shocks and cold fronts in the ICM that is complementary to X-rays.

Key words. radiation mechanisms: nonthermal – galaxies: clusters: intracluster medium – galaxies: clusters: general – acceleration of particles – shock waves

1. Introduction

The intra-cluster medium (ICM) is an X-ray-luminous ($\sim 10^{44}$ erg s⁻¹ in the 0.1–2.4 keV band), hot ($T \sim 10^8$ K), and tenuous ($n_e \sim 10^{-3}$ particles cm⁻³) plasma that comprises $\sim 75\%$ of the baryonic mass of galaxy clusters (e.g., Sarazin 1986). It acquires its high temperature from the energy released during the formation process of clusters, where gravitational energy is dissipated by shocks and large-scale turbulent motions and goes mainly into heating the ICM (e.g., Norman & Bryan 1999; Ricker & Sarazin 2001). A small fraction of the kinetic energy dissipated in cluster mergers is eventually channeled into nonthermal components (relativistic particles and magnetic fields), generating cluster-scale synchrotron sources (e.g., Brunetti & Jones 2014; van Weeren et al. 2019, for reviews).

One of the major findings of galaxy cluster science enabled by the superb angular resolution of *Chandra* is the characterization of sharp X-ray surface brightness discontinuities in the ICM due to shocks and cold fronts (e.g., Markevitch et al. 2000; Vikhlinin et al. 2001; Markevitch et al. 2002). These features

play an important role in our understanding of different aspects of the physics that governs the thermal gas (e.g., the plasma equipartition time, heat conductivity, and viscosity) as well as the processes that appear to be responsible for the generation of the nonthermal components mixed therein. For example, *Chandra* helped to establish the spatial coincidence between: radio relics and shock fronts in cluster outskirts (e.g., Giacintucci et al. 2008; Macario et al. 2011; Shimwell et al. 2015; Botteon et al. 2016a); the boundaries of radio mini-halos and sloshing cold fronts (e.g., Mazzotta & Giacintucci 2008; Giacintucci et al. 2014a,b); and the edges in the brightness distribution of some radio halos and X-ray-detected shocks (e.g., Markevitch et al. 2005; Markevitch 2010; Shimwell et al. 2014). These results demonstrate the interplay between nonthermal components and dynamical motions in the ICM, whose signatures in the thermal gas can only be efficiently unveiled when X-ray images reach sufficiently high resolution and sufficient count statistics are available.

Historically, the morphology of diffuse radio sources in the ICM has generally been observed as smooth in appearance. This

Table 1. List of the galaxy clusters in the MGCLS that host a radio halo. Elongated halos and halos with embedded bright AGN sources are indicated with a dagger symbol. All values are from Knowles et al. (2022). Abell 85 is included in the list because it hosts a type of diffuse emission bridging both halo and mini-halo classifications (see Knowles et al. 2022).

Cluster name	RA [deg]	Dec [deg]	z	LAS [arcmin]	LLS [Mpc]	rms [$\mu\text{Jy beam}^{-1}$]	Beam [" \times "]
Abell 85 [†]	10.453	-9.318	0.056	4.0	0.26	3.3	7.7×7.6
Abell 209	22.990	-13.576	0.209	7.9	1.62	3.6	7.8×7.7
Abell 521	74.536	-10.244	0.248	5.3	1.23	3.4	8.5×7.9
Abell 545b	83.102	-11.543	0.154	4.7	0.75	3.1	8.3×8.0
Abell 2667 [†]	357.920	-26.084	0.232	4.6	1.02	2.7	7.6×7.5
Abell 2744	3.567	-30.383	0.307	7.5	2.04	2.9	7.1×7.1
Abell 2811	10.537	-28.536	0.108	5.2	0.62	2.6	9.2×8.3
Abell 3558	201.978	-31.492	0.048	4.5	0.25	2.9	7.4×7.2
Abell 3562	202.783	-31.673	0.050	11.5	0.67	3.3	7.3×7.2
Abell S295	41.400	-53.038	0.300	4.0	1.07	2.3	8.1×7.9
Abell S1063	342.181	-44.529	0.348	5.5	1.62	2.6	7.1×7.0
Bullet Cluster	104.658	-55.950	0.297	8.5	2.26	2.8	7.9×7.6
El Gordo	15.719	-49.250	0.870	3.3	1.53	1.5	7.2×6.6
MACS J0417.5-1154 [†]	64.394	-11.909	0.443	4.9	1.68	2.9	7.9×7.8
RXC J1314.4-2525	198.599	-25.256	0.244	4.7	1.08	4.2	7.5×7.4
J0145.0-5300 (Abell 2941)	26.260	-53.014	0.117	4.9	0.62	2.6	7.5×7.4
J0225.9-4154 (Abell 3017)	36.478	-41.910	0.220	2.4	0.51	2.7	7.6×7.4
J0232.2-4420 (PSZ2 G259.98-63.43)	38.070	-44.348	0.286	5.8	1.49	2.6	7.5×7.3
J0303.7-7752 (PSZ1 G294.68-37.01)	45.943	-77.869	0.274	3.8	0.95	2.9	7.5×7.5
J0352.4-7401 (Abell 3186)	59.123	-74.031	0.127	10.7	1.46	2.6	7.8×7.6
J0516.6-5430 (Abell S520)	79.158	-54.514	0.295	5.7	1.51	3.1	7.7×7.4
J0528.9-3927 (Abell 3343)	82.235	-39.463	0.284	4.0	1.06	2.6	7.3×7.3
J0638.7-5358 (Abell S592) [†]	99.694	-53.972	0.227	6.4	1.40	3.4	7.3×7.2
J0645.4-5413 (Abell 3404)	101.372	-54.219	0.164	7.7	1.30	3.4	7.7×7.6
J1601.7-7544 (PSZ2 G313.88-17.11)	240.445	-75.746	0.153	5.9	0.94	3.7	8.5×7.8
J2023.4-5535 (PSZ1 G342.33-34.92)	305.852	-55.592	0.232	4.7	1.04	2.7	7.5×7.5

Notes. Col. 1: cluster name; Cols. 2 and 3: coordinates; Col. 4: redshift; Col. 5: largest angular size; Col. 6: largest linear size; Cols. 7 and 8: noise and resolution of the MeerKAT image.

was likely due to limitations of the data used, which were only able to recover the extended faint emission at low resolution and with low signal-to-noise ratio (S/N). Indeed, deeper and higher resolution observations in recent years (mainly performed with the new generation of radio interferometers) have unveiled an increasing number of substructures in radio halos (e.g., A2255, Botteon et al. 2020, 2022b), mini-halos (e.g., Perseus Cluster, Gendron-Marsolais et al. 2017), and relics (e.g., Sausage Cluster, Di Gennaro et al. 2018; Toothbrush Cluster, Rajpurohit et al. 2018; A2256, Owen et al. 2014; Rajpurohit et al. 2022; A3667, de Gasperin et al. 2022). Understanding the origin of these features may provide important insights into the generation, distribution, and evolution of cosmic rays and magnetic fields in the ICM. As particle acceleration of thermal electrons is an inefficient process, a preexisting population of mildly relativistic seed electrons in the ICM is required to produce the observed level of synchrotron emission in clusters (e.g., Brunetti & Jones 2014). In the case of radio halos, the seed electrons are believed to be re-accelerated in situ by the turbulence injected during mergers (e.g., Brunetti et al. 2001; Petrosian 2001; Fujita et al. 2003; Brunetti & Lazarian 2007, 2011, 2016; Pinzke et al. 2017; Nishiwaki & Asano 2022).

MeerKAT (Jonas 2009), located in South Africa, is a precursor of the Square Kilometer Array (SKA), and is to be integrated into the mid-frequency component of SKA in the future. With its 64 dishes, MeerKAT offers high sensitivity, dynamic range, and resolution, which, coupled with its densely populated core (48

antennas are concentrated within a diameter of ~ 1 km), provide exquisite image quality with which to study large-scale diffuse emission from clusters in great detail. While inspecting the recently released image at 1.28 GHz of the Bullet Cluster from the MeerKAT Galaxy Cluster Legacy Survey (MGCLS; Knowles et al. 2022), we noticed that in addition to the edge¹ of the radio halo emission already pointed out by Shimwell et al. (2014) but revealed in much more detail in the new MeerKAT image (see also Sikhosana et al. 2023), there are other surface brightness discontinuities in the radio halo. This motivated us to characterize them and search for similar edges in the entire sample of 26 radio halos detected in the MGCLS. In this paper, we present the results of this search. The paper is structured as follows. In Section 2 we provide details of the data used for the analysis. In Section 3, we describe the edge-detection technique(s) employed to search for discontinuities in the radio images. In Section 4, we present the results of our analysis of the Bullet Cluster and of our search for radio edges in the other radio halos in the sample. In Section 5, we discuss our findings and their implications. Finally, in Section 6, we summarize the most important results of our study. We assume a Λ cold dark matter cosmology with $\Omega_\Lambda = 0.7$, $\Omega_m = 0.3$, and $H_0 = 70 \text{ km s}^{-1} \text{ Mpc}^{-1}$ throughout.

¹ This is coincident with the famous shock front detected toward the west of the system (Markevitch et al. 2002).

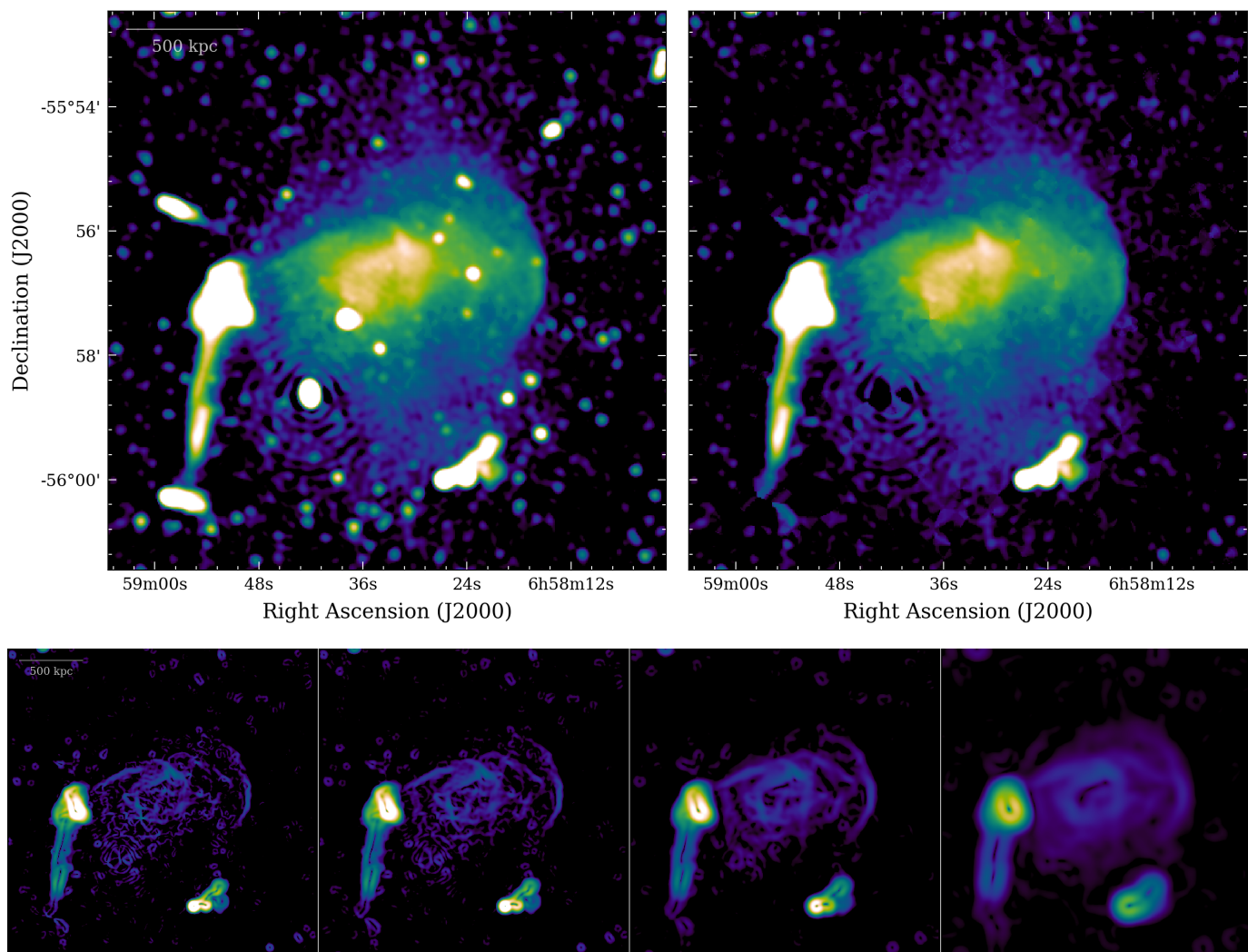


Fig. 1. Radio images of the Bullet Cluster. *Top panels:* MeerKAT image at 1.28 GHz of the radio halo with (left) and without (right) discrete sources. *Bottom panels:* GGM-filtered images obtained with $\sigma = 1, 2, 4,$ and 8 pixels (from left to right).

2. Data

2.1. MeerKAT

The MGCLS (Knowles et al. 2022) is a large program (~ 1000 h) consisting of observations of ~ 6 – 10 h in duration with MeerKAT *L*-band (900–1670 MHz) of 115 galaxy clusters in the southern sky. We used the full-resolution ($\sim 8''$) images that were made available with the first legacy product data release (DR1). These images have typical root-mean-square (rms) noise of ~ 2 – $5 \mu\text{Jy beam}^{-1}$ and reference frequency of 1.28 GHz. We retrieved these images for the Bullet Cluster and for the other 25 galaxy clusters reported to host a radio halo in Knowles et al. (2022) from the MGCLS website². The resolution and noise of the images used in this work are summarized in Table 1 together with the main properties of the clusters and halos studied. In all images, 1 pixel corresponds to $\sim 1.2''$ except for El Gordo in which 1 pixel is equal to $1.5''$.

Discrete radio sources interfere with the analysis of the diffuse emission in which they are embedded but this can be mitigated by removing them from the images. Subtracting discrete sources precisely is a difficult task and one of two different methods is generally adopted in the literature to perform this step. The

first method is to subtract the clean components of the discrete sources from the *uv* data and to reimage the subtracted visibilities to obtain source-subtracted images. In the second method, discrete sources are cosmetically removed directly from the images that contain them. The first approach confers the advantage that discrete sources and diffuse emission can be somewhat separated in interferometric data with sensitivity to a wide range of angular scales. However, the calibrated measurement sets are not available in the MGCLS-DR1 and performing the first procedure would require recalibration of all the data from raw visibilities. For this reason, we followed the second approach, the details of which are provided below.

MeerKAT 1.28 GHz images are extremely sensitive to the emission from active galactic nuclei (AGN), most of which are unresolved (e.g., Heywood et al. 2022). Source-detection algorithms such as Python Blob Detector and Source Finder (pyBDSF; Mohan & Rafferty 2015) and AEGEAN (Hancock et al. 2012, 2018) are generally useful to identify and characterize these compact sources. Nonetheless, in the presence of significant diffuse emission in the field-of-view (FoV) and/or AGN with extended and distorted morphology, which are conditions that both often occur in galaxy clusters, source detection is challenging and the automated packages can struggle to accurately character-

² <http://mgcls.sarao.ac.za/>

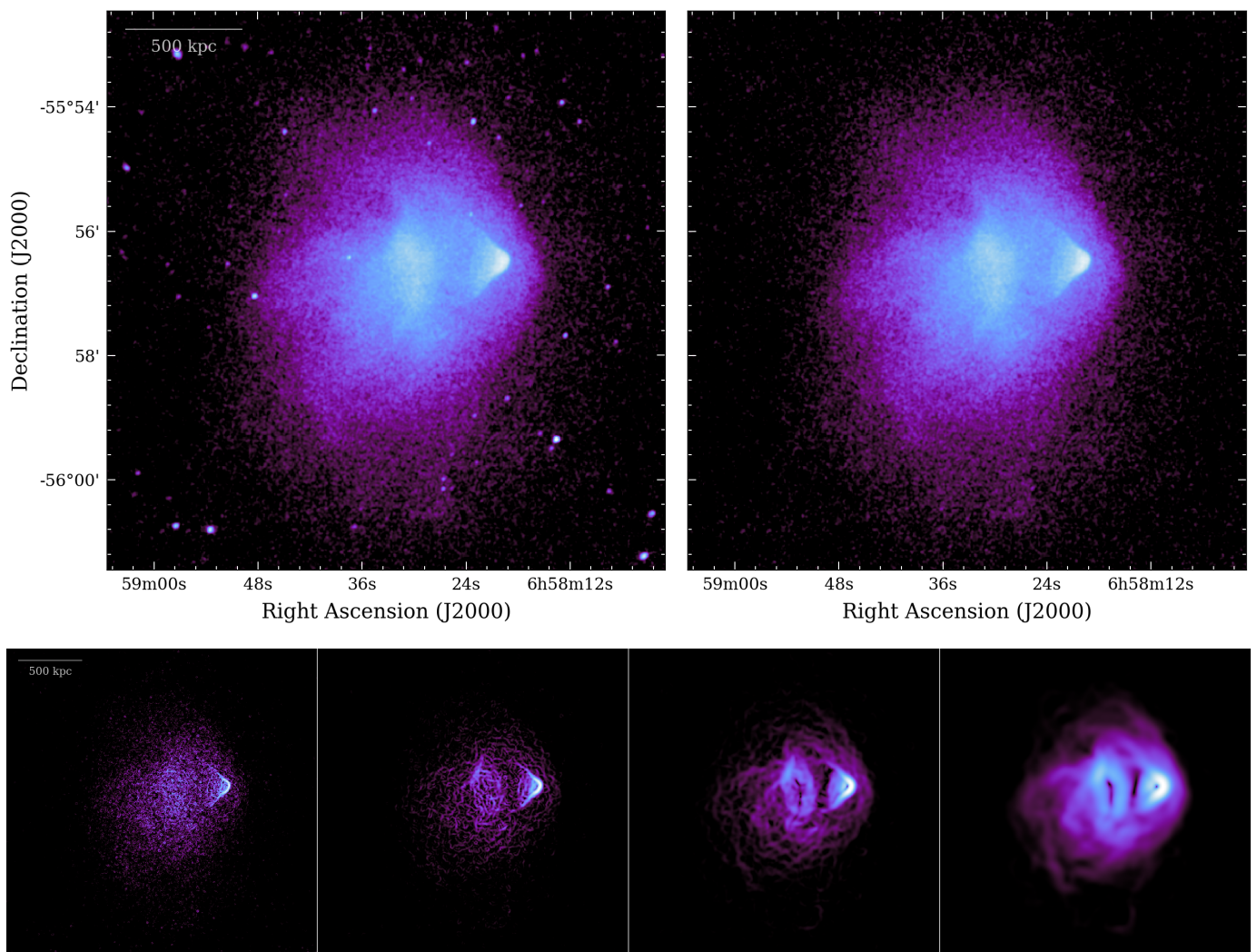


Fig. 2. X-ray images of the Bullet Cluster. *Top panels:* *Chandra* image in the 0.5–2.0 keV band of the thermal ICM with (*left*) and without (*right*) discrete sources. *Bottom panels:* GGM-filtered images obtained with $\sigma = 1, 2, 4, 8$ pixels (from *left to right*).

ize the emission from physically distinct but co-located objects. For this reason, we identified contaminating discrete sources by visually inspecting the radio images for local intensity peaks and drawing circular or elliptical region files encompassing the source emission. The visual search was carried out meticulously because of the small number of images to inspect (26, corresponding to the 26 galaxy clusters in our sample) and because we restricted the search to small regions covering the entire radio halo (the FoV typically inspected ranges from 0.03 to 0.22 deg²). Once identified, pixels inside the contaminating discrete source regions were first replaced with NaN values, then they were filled with values interpolated from neighboring data points assuming a 2D Gaussian kernel with the `interpolate_replace_nans` function from the `Astropy` package. A similar approach is commonly used in X-ray images (see e.g., the following subsection) and produces satisfactory results also in the radio images, as shown in the Fig. 1 (top panels). Still, we note in the case of very bright or extended sources it may introduce artifacts and remove any structure of the radio halo that may exist in the excised region. Depending on the specific case, we decided either to not remove difficult sources from the original images or to not consider in our analysis regions affected by subtraction (or calibration) artifacts that would lead to unreliable results.

2.2. *Chandra*

In this work, we also used archival *Chandra* ACIS-I observations of the Bullet Cluster (ObsIDs: 554, 3184, 4984, 4985, 4986, 5355, 5356, 5357, 5358, 5361). Data were processed using `CIAO` v4.13 (Fruscione et al. 2006) with `CALDB` v4.9.0 (Graessle et al. 2006) following standard data reduction procedures. The filtered exposure time amounts to ~ 517 ks. We produced exposure-corrected mosaic images of the cluster in the 0.5–2.0 keV energy band with and without point sources removed (Fig. 2, top panels). Point sources were automatically detected with the `wavdetect` task, visually validated, and thus cosmetically removed by replacing them with random values extracted from neighboring pixels. The pixel size in our *Chandra* images is $\sim 1''$.

3. Edge-detection techniques

Surface brightness discontinuities are regions characterized by sharp and significant brightness changes, and therefore gradient-filtering techniques are particularly useful in helping to identify them. Among the numerous edge-detection methods developed in digital image processing (e.g., Gonzalez & Woods 2002), the most commonly used are summarized below.

The *Prewitt/Roberts/Sobel* operators are based on first-order

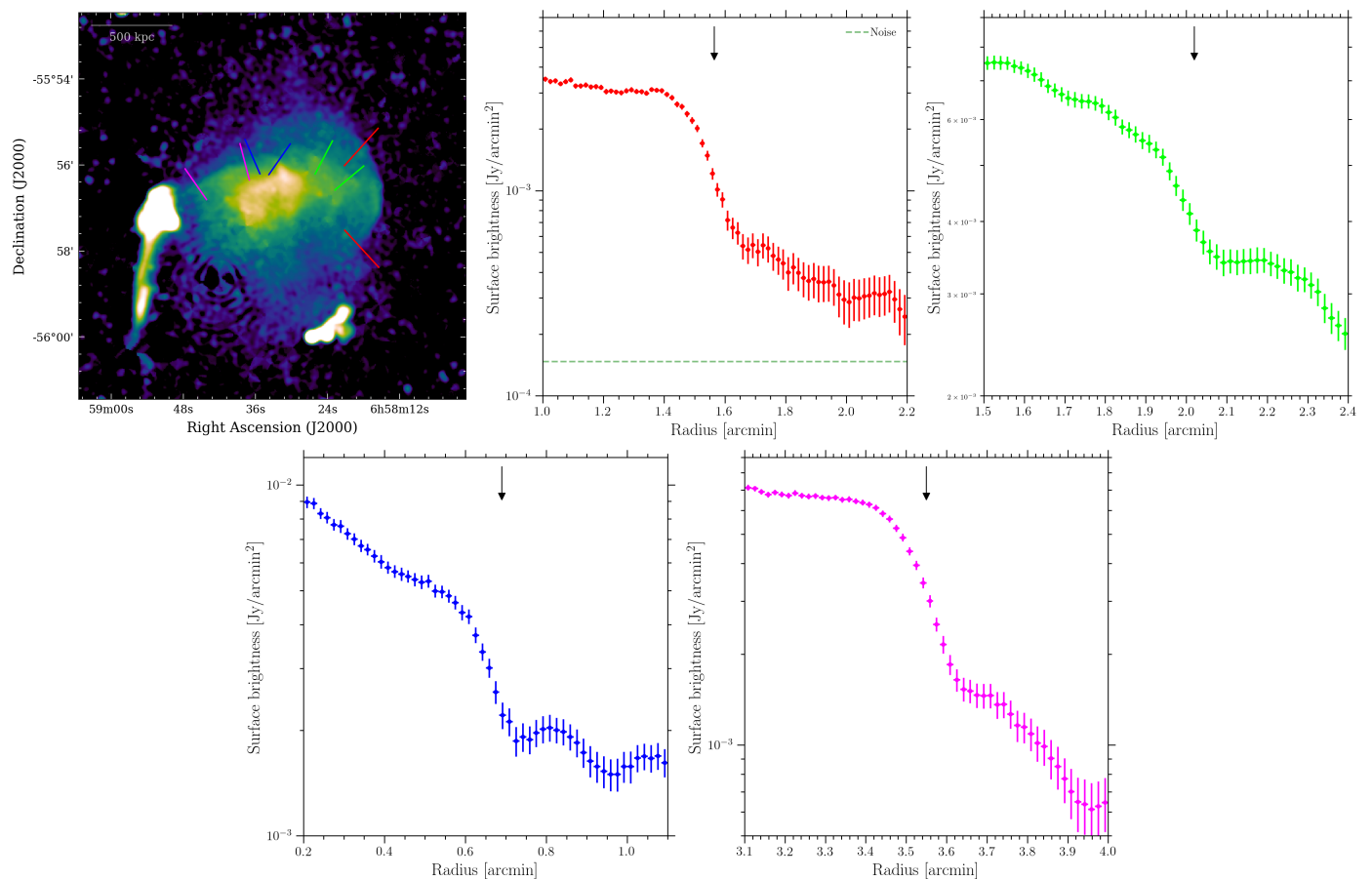


Fig. 3. Radio surface brightness profiles extracted from the discrete source-subtracted MeerKAT image of the Bullet Cluster across the most prominent features highlighted by the GGM-filtered images. Colored segments in the top-left panel denote the sectors used to extract the surface brightness profiles plotted following the same color scheme in the other panels of the figure. Arrows highlight the discontinuities in the profiles.

derivatives (Prewitt 1970; Roberts 1963; Sobel & Feldman 1968). They are discrete differentiation operators and differ in the approximation made to compute the gradient. The results of these filters are very similar.

The *Gaussian Gradient Magnitude* (GGM) filter uses Gaussian derivatives to compute the gradient. By changing the width of the Gaussian, it is possible to search for gradients over different scales.

The *Canny edge detection* is multi-step algorithm (Canny 1986). Firstly, the image is smoothed with a Gaussian to reduce noise. Secondly, a first-order derivative operator (generally Sobel) is used to find gradients. Thirdly, local maxima are searched for in the gradient image in order to thin out the edges (this step is called nonmaximum suppression). Finally, edge points between two thresholds are tracked by hysteresis and are then connected.

The *Laplace* operator is based on second-order derivatives (Marr & Hildreth 1980). Contrary to the techniques described above, this is a zero-crossing-based method (namely, edges are identified when the second derivative takes values of zero). The input image is often smoothed with a Gaussian before applying this filter to reduce noise.

The *unsharp mask* is obtained by subtracting an image smoothed with a wide Gaussian from the same image smoothed with a narrower Gaussian. This is a band-pass filter that is sensitive to spatial scales between the two adopted Gaussian widths.

The usage of a certain edge-detection method depends on the specific application and the characteristics of the image. Among these methods, the GGM filter is known to be robust to noise,

to produce thin edges, and to be computationally efficient. Thus, after a visual comparison with the results provided by the other algorithms (see bottom panels in Fig. 1 and Appendix A), we elected the GGM filter as the reference technique to aid our search for surface brightness discontinuities in radio halos. The advantage of this filter in applications to astronomical images (from *Chandra* and *XMM-Newton*) has already been pointed out in the literature (Sanders et al. 2016a; Walker et al. 2016), and consists in its flexibility when measuring gradients over more or fewer pixels depending on the scale of the features of interest and image S/N. Indeed, the GGM filter has been used intensively in X-ray images of galaxy clusters to find surface brightness edges associated with shocks and cold fronts (e.g., Sanders et al. 2016b, 2022; Walker et al. 2017, 2018; Botteon et al. 2018; Douglass et al. 2018; Schellenberger et al. 2019). To the best of our knowledge, it has not been applied yet to radio images of cluster diffuse synchrotron sources³.

The GGM-filtered images improve the clarity of surface brightness gradients whose presence would otherwise be assessed from unfiltered images using different contrasts and color scales in the region under investigation (Sanders et al. 2016a). We therefore selected the clearest features (namely, those following a coherent arc-shaped structure extending for ≥ 100 kpc in length; see e.g., Botteon et al. 2018) in the filtered images and

³ But the Sobel filter has been already used in the past in the study of radio galaxies (e.g., Murgia et al. 2001; Laing et al. 2011; Horellou et al. 2018; Ramatsoku et al. 2020; Condon et al. 2021; Rudnick et al. 2022).

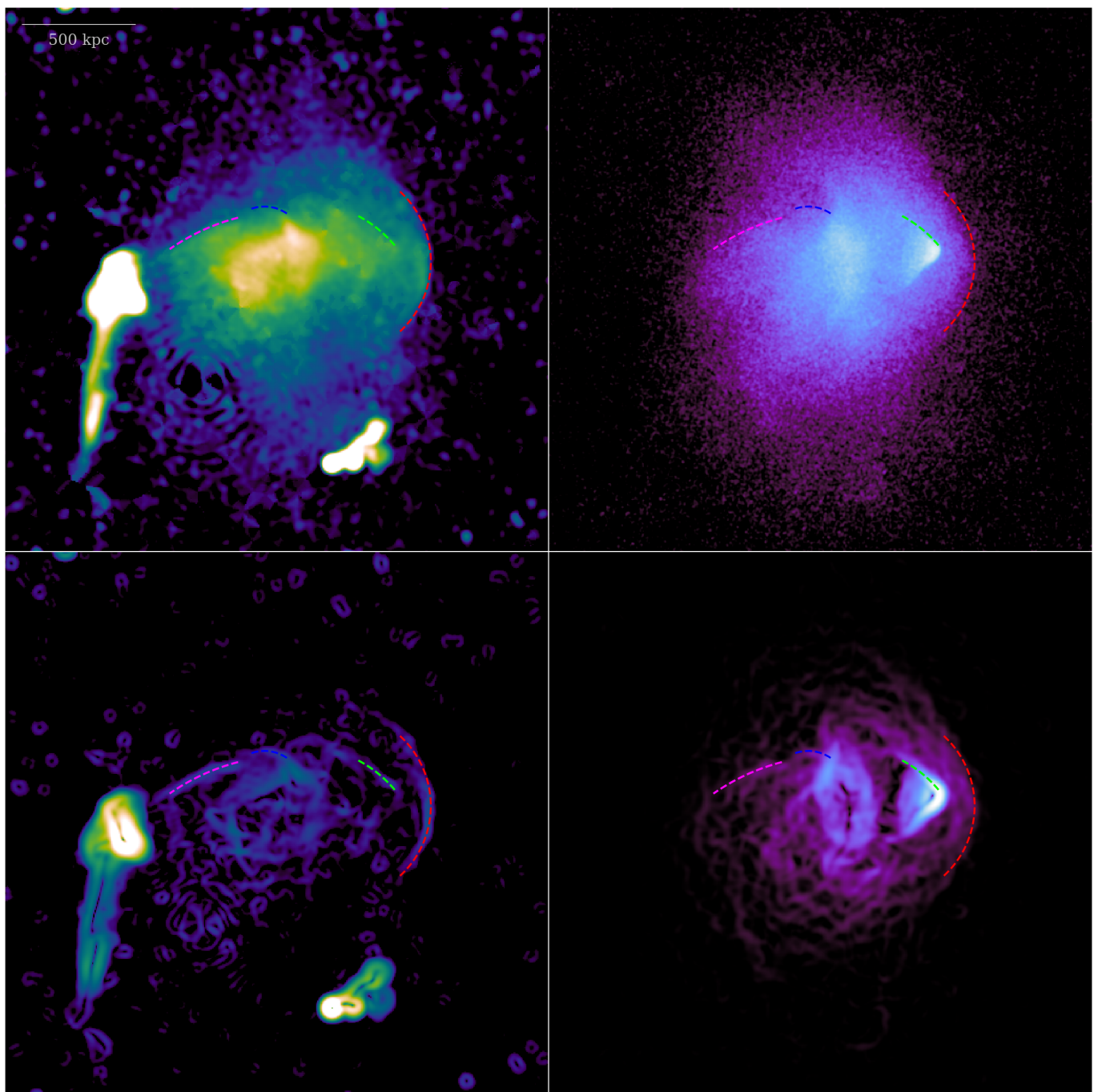


Fig. 4. MeerKAT and *Chandra* images of the Bullet Cluster (*top panels*) and corresponding GGM-filtered images (*bottom panels*). Dashed arcs mark the position and extent of the radio surface brightness discontinuities.

extracted surface brightness profiles across the identified edges from the discrete source-subtracted MeerKAT images using a version of `PYPROFFIT` (Eckert et al. 2020) that was modified to handle radio images with corresponding headers and units.

4. Results

4.1. The case of the Bullet Cluster

The Bullet Cluster (or 1E 0657–55.8) is one of the most massive ($M_{500} \approx 1.3 \times 10^{15} M_{\odot}$; Planck Collaboration XXVII 2016) and hottest ($kT \approx 17$ keV; Tucker et al. 1998) galaxy clusters observed and hosts the most luminous radio halo known (Liang

et al. 2000; Shimwell et al. 2014, 2015; Sikhosana et al. 2023). Due to its brightness, the diffuse radio emission from the ICM is detected at high S/N and is highly resolved in the MeerKAT image (Fig. 1, top panels), making it possible to search for subtle and small-scale morphological features. Similarly, the X-ray emission of the ICM is observed at high S/N thanks to the presence of deep *Chandra* observations (Fig. 2, top panels), which enable a direct comparison between the thermal and nonthermal emission of the system. Due to these high-quality detections, the Bullet Cluster is the obvious choice of system with which to begin our search for radio surface brightness discontinuities in radio halos.

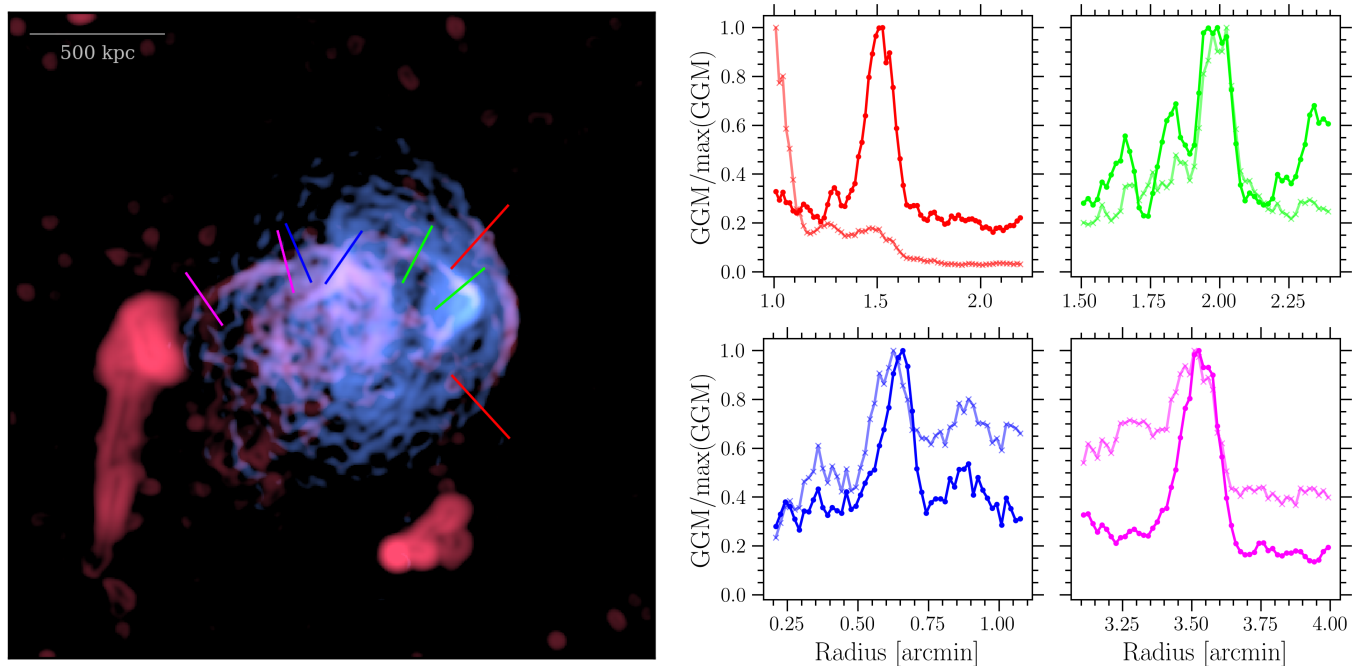


Fig. 5. Comparison between radio and X-ray surface brightness gradients. *Left panel:* Composite image of the gradients in the Bullet Cluster. The MeerKAT GGM-filtered image is reported in *red* while the *Chandra* GGM-filtered image is reported in *blue*. *Right panels:* Profiles extracted from the MeerKAT (*dots*, darker colors) and *Chandra* (*crosses*, lighter colors) GGM-filtered images in the four analyzed sectors, following the same color scheme. The profiles are normalized to the maximum value in the sector.

4.2. Radio surface brightness discontinuities

The MeerKAT image of the Bullet Cluster and the corresponding GGM-filtered images of Fig. 1 provide evidence for clear surface brightness discontinuities in the radio halo emission. To the west of the cluster, a strong and arc-shaped gradient marks the boundary of the radio halo. This edge is coincident with the shock front detected in the X-rays in the cluster (Markevitch et al. 2002; Markevitch 2006), where both radio and X-ray emissions abruptly drop. Additional radio gradients are observed in multiple directions; for example at the location of the cold front outlining the shoulder of the bullet following the western shock (Keshet et al. 2021) and in the northeast region of the cluster. A number of X-ray surface brightness gradients are also present in the *Chandra* GGM-filtered images (Fig. 2, bottom panels)

For a better visualization of the discontinuities, in Fig. 3 we report the radio surface brightness profiles extracted from the discrete source-subtracted image across the most prominent features highlighted by the GGM-filtered images. These profiles show rapid surface brightness declines over small scales. In the case of the western edge, which marks the strongest gradient, the radio surface brightness drops by a factor of ~ 6 – 7 within ~ 50 kpc (corresponding to ~ 1.5 resolution element). We note that all the profiles extracted during the analysis were obtained from sectors (whose radial extent and aperture are denoted by the colored segments in the top left panel of Fig. 3) with a linear binning of $1''$, which is smaller than the resolution of the radio image, meaning that edges are convolved with the beam size ($7.9'' \times 7.6''$) and thus in reality could be even sharper. The modeling of the profiles is beyond the scope of this paper, and will be the focus of a subsequent study.

4.3. Comparison with the ICM thermal emission

The shape of the radio surface brightness profiles shown in Fig. 3 is similar to that typically observed in the X-rays for shocks and cold fronts in the ICM (e.g., Markevitch & Vikhlinin 2007). It is therefore natural to check whether the radio edges are co-located with X-rays edges. In Fig. 4 we overlay the position of the radio surface brightness discontinuities onto the MeerKAT and *Chandra* images and corresponding GGM-filtered images of the cluster, while in Fig. 5 (left panel) we report an overlay between the radio and X-ray GGM-filtered images. These were obtained by smoothing the *Chandra* image to the resolution of the MeerKAT image, regriding them to the same pixelation, and applying the GGM filter with $\sigma = 1$ pixel. The correspondence between radio and X-rays edges is striking. To better visualize the correlation between the gradients in the two images, in the right panels of Fig. 5 we show the profiles extracted from the GGM-filtered images across the four radio discontinuities. Except for the western edge (shown in red in Fig. 5), the profiles are similar and, most importantly, they peak at the same position; that is, the radio and X-ray gradients are correlated. The western radio edge, which is associated with the famous shock front, appears different in radio and X-rays because the X-ray GGM profile across this discontinuity is contaminated at small radii by the strong gradient due to the cold front of the bullet subcluster. Nonetheless, we note that the X-ray GGM profile (which is normalized to its peak value) shows a bump at the radial distance at which we observe the maximum of the radio GGM profile. This bump is due to the strong shock front detected in X-rays by Markevitch et al. (2002), and therefore also in this case there is a coincidence between radio and X-ray gradients.

As anticipated, the western discontinuity (shown in red) traces the region of the radio halo that is bounded by the large bow shock (Shimwell et al. 2014), while the edge downstream (shown in green) is coincident with the cold front surrounding

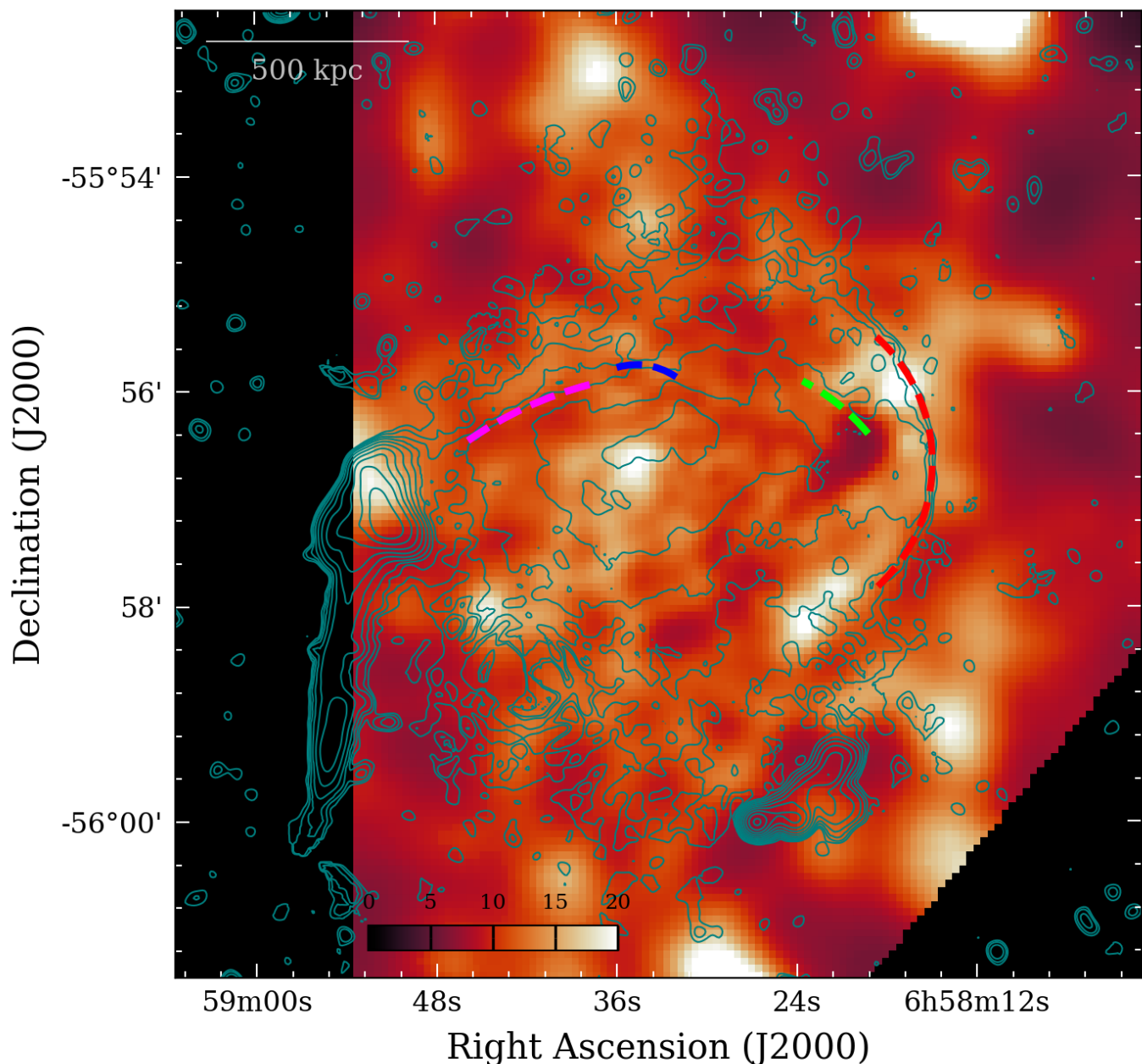


Fig. 6. Temperature map in keV units of the Bullet Cluster derived from the *Chandra* data following the method described in Markevitch et al. (2000) and Wang et al. (2016). Contours show the radio emission from the MeerKAT discrete source-subtracted image spaced by a factor of 2 starting from $3 \times \text{rms}$. Dashed arcs mark the positions of the radio surface brightness discontinuities. The corresponding error map is reported in Appendix. A.

the bullet head (Markevitch et al. 2002). The northeast discontinuity (shown in magenta) is prominent in the MeerKAT image and profile and is mirrored by an X-ray surface brightness gradient, which is observed more clearly in the *Chandra* GGM-filtered image. The presence of this X-ray edge has not been reported until now and we speculate it traces a cold front given that the thermal gas appears colder in its denser region (~ 10 keV, compared to $\sim 12\text{--}13$ keV of the outer region), as inferred from the temperature map of Fig. 6. The radio edge in the central region of the cluster (blue color) is associated with an X-ray gradient that is probably due to a large Kelvin-Helmholtz roll, where we expect amplified magnetic field due to shear velocity, which may explain the edge in the synchrotron emission.

Both the MeerKAT and *Chandra* GGM-filtered images show many prominent surface brightness structures in the middle of the cluster (Figs. 4 and 5). This central region likely traces the remnant of the bigger subcluster that has been disturbed by the high-speed passage of the bullet subcluster (Clowe et al. 2006).

4.4. Search for radio edges in the other MGCLS radio halos

The Bullet Cluster is one of the 26 galaxy clusters reported to host a radio halo in the MGCLS (Knowles et al. 2022). We expanded our search for radio surface brightness discontinuities in radio halos by applying the same techniques adopted for the Bullet Cluster to the remaining 25 galaxy clusters in the sample

(Table 1). Below we summarize the main results of our analysis. In Appendixes B and C, we report the images and radio surface brightness profiles for the clusters in which the GGM-filtered images highlight the presence or absence of surface brightness gradients in the radio halo emission, respectively.

In addition to the case of the Bullet Cluster, we find that at least one radio surface brightness gradient is present in another 12 radio halos. That is, 50% of the radio halos in the MGCLS may show edges. These additional clusters are: Abell 85, Abell 209, Abell 521, Abell 2744, Abell 3562, MACS J0417.5-1155, RXC J1314.4-2525, J0225.9-4154, J0232.2-4420, J0638.7-5358, J0645.4-5413, and J2023.4-5535 (see Appendix B). Multiple gradients are noted in 4 out of these 12 clusters. Many of the gradients observed show surface brightness profiles similar to that of the Bullet Cluster, while others are more subtle (i.e., the surface brightness jump is shallower and/or the profile shows fluctuations), which make any firm claim of an edge less obvious. Surface brightness jumps at the boundary of halos detected with low S/N should be taken with particular care, as in these noisy regions the extended radio emission may not be accurately reconstructed by the CLEAN algorithm. Overall, we extracted radio surface brightness profiles across 16 sectors (20, if we include those in the Bullet Cluster). We anticipate that, in general, the radio halos in which we do not observe surface brightness gradients are those detected with lower S/N in the MeerKAT images (see Appendix C). We return to this point at the end of Section 5.

5. Discussion

Surface brightness edges in the cluster X-ray emission have now been observed in numerous systems (e.g., Markevitch & Vikhlinin 2007; Owers et al. 2009; Ghizzardi et al. 2010; Markevitch 2010; Walker et al. 2016; Botteon et al. 2018, for collections). These edges trace density contrasts associated with shocks and cold fronts generated during cluster mergers, sloshing motions, or AGN outbursts. In contrast, only a handful of discontinuities in radio halos have been observed to date. The most striking cases are: Abell 520 (Markevitch et al. 2005; Vacca et al. 2014; Wang et al. 2018; Hoang et al. 2019), Coma Cluster (Brown & Rudnick 2011; Bonafede et al. 2022), Bullet Cluster (Shimwell et al. 2014; Sikhosana et al. 2023), and Toothbrush Cluster (van Weeren et al. 2016; Rajpurohit et al. 2018). In these clusters, the radio halo emission is bounded by a front that is coincident with an underlying X-ray-confirmed shock (see also Markevitch 2010). Thanks to the high quality of the new MeerKAT data and the deep archival *Chandra* observations, the Bullet Cluster can be considered a textbook example of a radio halo–shock connection.

In addition to the well-known edge, the MeerKAT image and corresponding GGM-filtered images of the Bullet Cluster allowed us to pinpoint additional surface brightness discontinuities in the radio halo emission. These gradients are also detected in the inner regions of the cluster, and are associated with discontinuities in the X-ray emission. Clear surface brightness jumps in the diffuse radio emission were found in other galaxy clusters of the studied sample, indicating that the Bullet Cluster is not unique in showing this kind of feature. Although not all the clusters in the sample have been targeted with (deep) X-ray observations, we note that some of the radio edges found are co-located with shocks and cold fronts claimed in previous studies, such as those in Abell 85 (Ichinohe et al. 2015; Rahaman et al. 2022), Abell 2744 (Owers et al. 2011; Jauzac et al. 2016), MACS J0417.5-1155 (Botteon et al. 2018; Pandge et al. 2019), J0225.9-

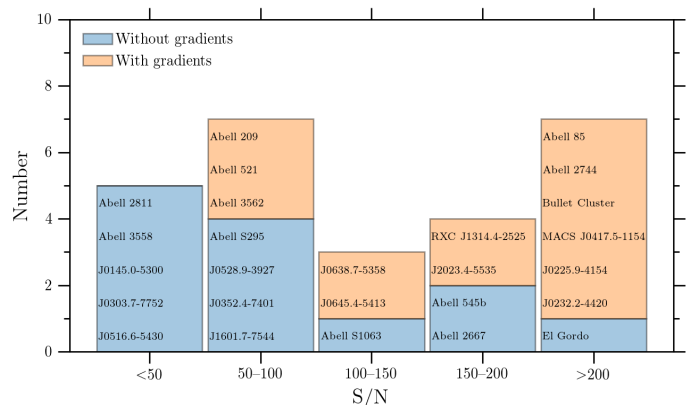


Fig. 7. Distribution of the S/N for the radio halos in the MGCLS grouped according to the presence or absence of radio surface brightness gradients.

4154 (Chon et al. 2019), and J0638.7-5358 (Botteon et al. 2018). These results suggest that the dynamical motions in the ICM induced by the ongoing merger activity shape the morphology of both the thermal and nonthermal cluster emissions and that these components are tightly related. This is probably due to the fact that the magnetic field is largely frozen into the thermal plasma and is advected, with gas flows in the ICM dragging the enclosed cosmic rays.

In Fig. 7 we grouped the clusters in the sample according to the S/N of their radio halo and to the presence of radio surface brightness gradients. The S/N was evaluated as $S/(\text{rms} \sqrt{N_b})$, where S is the flux density of the radio halo and N_b is the number of beams covered by the diffuse emission. This plot highlights that surface brightness gradients in radio halos are preferentially found in the clusters detected at higher S/N in the MeerKAT images. For example, the five clusters in which we detect multiple radio gradients (Bullet Cluster, Abell 2744, MACS J0417.5-1155, RXC J1314.4-2525, and J0225.9-4154) are among the cases where the radio halo emission is detected at higher S/N, while the 13 clusters where we do not find any radio gradient have generally lower S/N. This could indicate observational bias, in which radio surface brightness discontinuities may be common but may only be detected when the data used have a sufficient S/N.

5.1. Implications

Whether or not all radio edges trace shocks and cold fronts in the ICM needs to be confirmed in the future. With the current analysis, we can state that at least some of them are co-located with X-ray discontinuities. Radio edges without an X-ray counterpart may trace specific regions in the ICM that are abundant in seed relativistic electrons or where the acceleration efficiency or magnetic field strength are locally enhanced. For the Bullet Cluster, we pointed out that the northeast radio surface brightness jump is possibly associated with a cold front that was not claimed in past studies. This provides a tantalizing indication that surface brightness gradients in radio halos could be helpful for the discovery of new shocks and cold fronts in the ICM. Moreover, comparisons of the typical duration of the observations in the MGCLS (~6–10 h) with the long exposures of the deep *Chandra* observations required to detect X-ray discontinuities in the ICM (i.e., ≥ 50 ks ≈ 14 h, but more generally >100 ks) suggest new radio observations appear more efficient in this task. Radio data have already guided X-ray observations in the search for

shock fronts in cluster outskirts associated with previously detected radio relics (e.g., [Finoguenov et al. 2010](#); [Macario et al. 2011](#); [Akamatsu et al. 2012](#); [Akamatsu & Kawahara 2013](#); [Bourdoin et al. 2013](#); [Shimwell et al. 2015](#); [Botteon et al. 2016a,b](#); [Eckert et al. 2016](#); [Urdampilleta et al. 2018, 2021](#); [Di Gennaro et al. 2019](#); [Ge et al. 2019](#)). Thanks to the high-resolution and sensitive imaging enabled by MeerKAT, it now appears possible to expand the search for features related to the dynamics of the ICM to the inner regions of clusters using radio halos.

High-resolution (i.e., $\lesssim 10''$) imaging of extended radio sources was not possible until recently because of the requirement for very high surface brightness sensitivity at high angular resolution. Observing radio halos and relics with unprecedented resolution has the potential to transform our understanding of the physical processes leading to the formation of these extended sources. With the discovery of numerous radio edges, it appears that the historical definition of radio halos as “smooth” sources with “regular” morphology (see [Feretti et al. 2012](#); [van Weeren et al. 2019](#), for the definition of radio halo) is no longer valid: our results indicate that radio halos are rich in substructure.

The azimuthal surface brightness profiles of radio halos is usually described with an exponential function (e.g., [Murgia et al. 2009](#); [Boxelaar et al. 2021](#)). The reasons for the choice of this profile shape are twofold: it is a simple function with only two free parameters, and it provides a reasonable description of many radio halos (despite not being physically motivated). It is clear that once a high S/N is achieved, substructures in the diffuse radio emission become more evident and this model provides poorer fitting statistics. This was recently pointed out by [Botteon et al. \(2022a\)](#), who fitted 73 radio halos observed with LOFAR finding that those detected at higher S/N are those that show larger deviations from the exponential profile (see Appendix A for the residuals obtained for the Bullet Cluster). This is similar to previous findings for X-rays, where the β -model ([Cavaliere & Fusco-Femiano 1976](#)) was customarily used to fit the X-ray surface brightness profiles of clusters with low-resolution satellites (e.g., *Einstein*, *ASCA*, *ROSAT*), but with the advent of higher resolution instruments (such as *Chandra* and *XMM-Newton*), numerous substructures due to shocks, cold fronts, and cavities became evident, indicating that cluster atmospheres are very dynamic and that their profiles cannot be properly described by a smooth model. The presence of edges in radio halos will naturally lead to large deviations if the azimuthal profiles of these sources are fitted with an exponential model.

5.2. Prospects

Here we present the first identification of surface brightness gradients and the extraction of the corresponding profiles in a sample of radio halos. The natural follow-up to this work is the modeling of the profiles and the simultaneous analysis of the thermal and nonthermal emissions. In X-rays, a projection of a 3D spherical discontinuity is generally adopted to describe the underlying density profile for the surface brightness jumps associated with shocks and cold fronts. This model is motivated by the fact that these edges mark contrasts in the thermal electron density n_e and that the X-ray emissivity in the hot ($\gtrsim 2.5$ keV) ICM is $j_x \propto n_e^2 (kT)^{1/2}$, which is very weakly dependent on the gas temperature in the soft X-ray band (e.g., [Ettori 2000](#)). In radio, the synchrotron emissivity at frequency ν for a simple power-law spectrum is $j_r \propto n_{\text{CRE}} B^{(\delta+1)/2} \nu^{-(\delta-1)/2}$, and therefore depends on the magnetic field strength B , the density of the emitting nonthermal electrons n_{CRE} , and the slope of the electron energy distribution δ (which is related to the observed synchrotron spectrum

via $\delta = 2\alpha + 1$). Therefore, determining what causes the jump is not trivial, because of the degeneracy between n_{CRE} and B . Additional effects related to the properties of the magnetic field and processes taking place in the ICM (e.g., stretching, compression, and amplification) have an impact on the emissivity, radiative losses, and reacceleration rate of nonthermal electrons, making the situation even more complex (e.g., [Brunetti & Vazza 2020](#); [Chibueze et al. 2021](#); [Rudnick et al. 2022](#)). In addition, the modeling of the extracted profiles must account for the beam size, which artificially smears the surface brightness discontinuities (assuming that edges are sharper than the resolution of the radio images).

Although the count statistics of the available X-ray observations for the clusters in the studied sample is generally lower than that for the Bullet Cluster, previous studies have already reported the presence of shocks and cold fronts at the positions of several of the radio edges we discovered in this study (see discussion above). The majority of the radio discontinuities observed currently lack a counterpart in X-rays and our results can aid future studies to search for the associated edges in the thermal gas distribution in the archival data or eventually to propose targeted follow-up observations.

6. Conclusions

We used a recently published MeerKAT image at 1.28 GHz of the Bullet Cluster from the MGCLS to detect four surface brightness discontinuities in the radio halo emission. The presence of these edges was highlighted thanks to the GGM filter, which has proven to be helpful in the identification of these features in the diffuse radio emission (previously, this filter was applied to cluster X-ray images to facilitate the detection of shocks and cold fronts). The surface brightness profiles extracted across the radio gradients are very similar to those obtained in X-rays for cluster shocks and cold fronts reported in the literature. The four radio edges observed in the Bullet Cluster are coincident with X-ray gradients. This suggests that the magnetic field frozen into the ICM mediates the coupling between nonthermal and thermal particles and that the morphology of the radio and X-ray cluster emissions is shaped by the dynamical motions of the gas during the merger.

By applying the same techniques adopted for the Bullet Cluster to the other 25 radio halos in the MGCLS, we find that half of the clusters in the sample show at least one radio surface brightness gradient. The fact that edges are more frequent and more clear in halos detected at higher S/N (such as the Bullet Cluster and Abell 2744) indicates that high-quality images are necessary to characterize the discontinuities, and also that these edges may be common in radio halos but their presence could be hindered when the radio emission is observed with low S/N.

In general, the results of this work imply that the emission of radio halos is not smooth, but rich in substructure arising from complex motions in the ICM. We are able to make this claim thanks to the high resolution and sensitivity provided by the MeerKAT images. In the future, we expect that radio surface brightness discontinuities in radio halos will be routinely observed thanks to the new generation of instruments, which may provide a more efficient means to detect shocks and cold fronts in the ICM than X-ray observations.

Acknowledgements. We thank the anonymous referee for providing constructive comments to improve the presentation of the results. RJvW acknowledges support from the ERC Starting Grant ClusterWeb 804208. MGCLS data products were provided by the South African Radio Astronomy Observatory and the MGCLS team and were derived from observations with the MeerKAT ra-

dio telescope. The MeerKAT telescope is operated by the South African Radio Astronomy Observatory, which is a facility of the National Research Foundation, an agency of the Department of Science and Innovation. This research made use of APLpy, an open-source plotting package for Python (Robitaille & Bressert 2012), and Astropy, a community-developed core Python package and an ecosystem of tools and resources for astronomy (Astropy Collaboration et al. 2013, 2018). Parts of the results in this work make use of the colormaps in the CMasher package (van der Velden 2020).

References

- Akamatsu, H. & Kawahara, H. 2013, PASJ, 65, 16
- Akamatsu, H., Takizawa, M., Nakazawa, K., et al. 2012, PASJ, 64, 67
- Astropy Collaboration, Price-Whelan, A. M., Sipőcz, B. M., et al. 2018, AJ, 156, 123
- Astropy Collaboration, Robitaille, T. P., Tollerud, E. J., et al. 2013, A&A, 558, A33
- Bonafede, A., Brunetti, G., Rudnick, L., et al. 2022, ApJ, 933, 218
- Botteon, A., Brunetti, G., van Weeren, R. J., et al. 2020, ApJ, 897, 93
- Botteon, A., Gastaldello, F., & Brunetti, G. 2018, MNRAS, 476, 5591
- Botteon, A., Gastaldello, F., Brunetti, G., & Dallacasa, D. 2016a, MNRAS, 460, L84
- Botteon, A., Gastaldello, F., Brunetti, G., & Kale, R. 2016b, MNRAS, 463, 1534
- Botteon, A., Shimwell, T. W., Cassano, R., et al. 2022a, A&A, 660, A78
- Botteon, A., van Weeren, R. J., Brunetti, G., et al. 2022b, Science Adv., 8, eabq7623
- Bourdin, H., Mazzotta, P., Markevitch, M., Giacintucci, S., & Brunetti, G. 2013, ApJ, 764, 82
- Boxelaar, J. M., van Weeren, R. J., & Botteon, A. 2021, A&C, 35, 100464
- Brown, S. & Rudnick, L. 2011, MNRAS, 412, 2
- Brunetti, G. & Jones, T. W. 2014, IJMPD, 23, 30007
- Brunetti, G. & Lazarian, A. 2007, MNRAS, 378, 245
- Brunetti, G. & Lazarian, A. 2011, MNRAS, 412, 817
- Brunetti, G. & Lazarian, A. 2016, MNRAS, 458, 2584
- Brunetti, G., Setti, G., Feretti, L., & Giovannini, G. 2001, MNRAS, 320, 365
- Brunetti, G. & Vazza, F. 2020, Phys. Rev. Lett., 124, 51101
- Canny, J. 1986, IEEE Trans. Pattern Anal. Mach. Intell., PAMI-8, 679
- Cavaliere, A. & Fusco-Femiano, R. 1976, A&A, 49, 137
- Chibueze, J. O., Sakemi, H., Ohmura, T., et al. 2021, Nature, 593, 47
- Chon, G., Böhringer, H., Dasadia, S., et al. 2019, A&A, 621, A77
- Clowe, D., Bradač, M., Gonzalez, A. H., et al. 2006, ApJ, 648, L109
- Condon, J., Cotton, W., White, S. V., et al. 2021, ApJ, 917, 18
- de Gasperin, F., Rudnick, L., Finoguenov, A., et al. 2022, A&A, 659, A146
- Di Gennaro, G., van Weeren, R. J., Andrade-Santos, F., et al. 2019, ApJ, 873, 64
- Di Gennaro, G., van Weeren, R. J., Hoeft, M., et al. 2018, ApJ, 865, 24
- Douglass, E., Blanton, E. L., Randall, S. W., et al. 2018, ApJ, 868, 121
- Eckert, D., Finoguenov, A., Ghirardini, V., et al. 2020, Open J. Astrophys., 3, 12
- Eckert, D., Jauzac, M., Vazza, F., et al. 2016, MNRAS, 461, 1302
- Ettori, S. 2000, MNRAS, 311, 313
- Feretti, L., Giovannini, G., Govoni, F., & Murgia, M. 2012, A&A Rev., 20, 54
- Finoguenov, A., Sarazin, C. L., Nakazawa, K., Wik, D. R., & Clarke, T. E. 2010, ApJ, 715, 1143
- Fruscione, A., McDowell, J. C., Allen, G. E., et al. 2006, Society of Photo-Optical Instrumentation Engineers (SPIE) Conference Series, Vol. 6270, CIAO: Chandra's data analysis system, 62701V
- Fujita, Y., Takizawa, M., & Sarazin, C. L. 2003, ApJ, 584, 190
- Ge, C., Sun, M., Liu, R.-Y., et al. 2019, MNRAS, 486, L36
- Gendron-Marsolaïs, M.-L., Hlavacek-Larrondo, J., van Weeren, R. J., et al. 2017, MNRAS, 469, 3872
- Ghizzardi, S., Rossetti, M., & Molendi, S. 2010, A&A, 516, A32
- Giacintucci, S., Markevitch, M., Brunetti, G., et al. 2014a, ApJ, 795, 73
- Giacintucci, S., Markevitch, M., Venturi, T., et al. 2014b, ApJ, 781, 9
- Giacintucci, S., Venturi, T., Macario, G., et al. 2008, A&A, 486, 347
- Gonzalez, R. C. & Woods, R. E. 2002, Digital image processing
- Graessle, D. E., Evans, I. N., Glotfelty, K., et al. 2006, in Society of Photo-Optical Instrumentation Engineers (SPIE) Conference Series, Vol. 6270, Society of Photo-Optical Instrumentation Engineers (SPIE) Conference Series., ed. D. R. Silva & R. E. Doxsey, 62701X
- Hancock, P. J., Murphy, T., Gaensler, B. M., Hopkins, A., & Curran, J. 2012, MNRAS, 422, 1812
- Hancock, P. J., Trott, C. M., & Hurley-Walker, N. 2018, PASA, 35, e011
- Heywood, I., Jarvis, M., Hale, C. L., et al. 2022, MNRAS, 509, 2150
- Hoang, D. N., Shimwell, T. W., van Weeren, R. J., et al. 2019, A&A, 622, A20
- Horellou, C., Intema, H. T., Smolčić, V., et al. 2018, A&A, 620, A19
- Ichinohe, Y., Werner, N., Simionescu, A., et al. 2015, MNRAS, 448, 2971
- Jauzac, M., Eckert, D., Schwinn, J., et al. 2016, MNRAS, 463, 3876
- Jonas, J. 2009, IEEE Proceedings, 97, 1522
- Keshet, U., Raveh, I., & Naor, Y. 2021, MNRAS, 508, 3455
- Knowles, K., Cotton, W., Rudnick, L., et al. 2022, A&A, 657, A56
- Laing, R., Guidetti, D., Bridle, A., Parma, P., & Bondi, M. 2011, MNRAS, 417, 2789
- Liang, H., Hunstead, R. W., Birkinshaw, M., & Andreani, P. 2000, ApJ, 544, 686
- Macario, G., Markevitch, M., Giacintucci, S., et al. 2011, ApJ, 728, 82
- Markevitch, M. 2006, in ESA Special Publication, Vol. 604, The X-ray Universe 2005, ed. A. Wilson, 723
- Markevitch, M. 2010, arXiv e-prints [arXiv:1010.3660]
- Markevitch, M., Gonzalez, A. H., David, L. P., et al. 2002, ApJ, 567, L27
- Markevitch, M., Govoni, F., Brunetti, G., & Jerius, D. 2005, ApJ, 627, 733
- Markevitch, M., Ponman, T. J., Nulsen, P. E., et al. 2000, ApJ, 541, 542
- Markevitch, M. & Vikhlinin, A. 2007, Phys. Rep., 443, 1
- Marr, D. & Hildreth, E. 1980, Proc. R. Soc. London Ser. B, 207, 187
- Mazzotta, P. & Giacintucci, S. 2008, ApJ, 675, L9
- Mohan, N. & Rafferty, D. 2015, PyBDSF: Python Blob Detection and Source Finder, Astrophysics Source Code Library
- Murgia, M., Govoni, F., Markevitch, M., et al. 2009, A&A, 499, 679
- Murgia, M., Parma, P., de Ruiter, H., et al. 2001, A&A, 380, 102
- Nishiwaki, K. & Asano, K. 2022, ApJ, 934, 182
- Norman, M. L. & Bryan, G. L. 1999, in Lecture Notes in Physics, Berlin Springer Verlag, Vol. 530, The Radio Galaxy Messier 87, ed. H.-J. Röser & K. Meisenheimer, 106
- Owen, F. N., Rudnick, L., Eilek, J. A., et al. 2014, ApJ, 794, 24
- Owers, M. S., Nulsen, P. E., Couch, W. J., & Markevitch, M. 2009, ApJ, 704, 1349
- Owers, M. S., Randall, S. W., Nulsen, P. E., et al. 2011, ApJ, 728, 27
- Pandge, M., Monteiro-Oliveira, R., Bagchi, J., et al. 2019, MNRAS, 482, 5093
- Petrosian, V. 2001, ApJ, 557, 560
- Pinzke, A., Oh, S., & Pfrommer, C. 2017, MNRAS, 465, 4800
- Planck Collaboration XXVII. 2016, A&A, 594, A27
- Prewitt, J. M. S. 1970, Pict. Process. and Psychopictorics
- Rahaman, M., Raja, R., Datta, A., Burns, J. O., & Rapetti, D. 2022, MNRAS, 515, 2245
- Rajpurohit, K., Hoeft, M., van Weeren, R. J., et al. 2018, ApJ, 852, 65
- Rajpurohit, K., van Weeren, R. J., Hoeft, M., et al. 2022, ApJ, 927, 80
- Ramatsoku, M., Murgia, M., Vacca, V., et al. 2020, A&A, 636, L1
- Ricker, P. & Sarazin, C. L. 2001, ApJ, 561, 621
- Roberts, L. G. 1963, PhD thesis, Massachusetts Institute of Technology
- Robitaille, T. P. & Bressert, E. 2012, APLpy: Astronomical Plotting Library in Python, Astrophysics Source Code Library
- Rudnick, L., Brügggen, M., Brunetti, G., et al. 2022, ApJ, 935, 168
- Sanders, J. S., Biffi, V., Brügggen, M., et al. 2022, A&A, 661, A36
- Sanders, J. S., Fabian, A. C., Russell, H. R., Walker, S. A., & Blundell, K. M. 2016a, MNRAS, 460, 1898
- Sanders, J. S., Fabian, A. C., Taylor, G. B., et al. 2016b, MNRAS, 457, 82
- Sarazin, C. L. 1986, Rev. Mod. Phys., 58, 1
- Schellenberger, G., David, L. P., O'Sullivan, E., Vrtilik, J. M., & Haines, C. P. 2019, ApJ, 882, 59
- Shimwell, T. W., Brown, S., Feain, I., et al. 2014, MNRAS, 440, 2901
- Shimwell, T. W., Markevitch, M., Brown, S., et al. 2015, MNRAS, 449, 1486
- Sikhosana, S. P., Knowles, K., Hilton, M., Moodley, K., & Murgia, M. 2023, MNRAS, 518, 4595
- Sobel, I. & Feldman, G. M. 1968, in Stanford Artif. Intell. Proj.
- Tucker, W., Blanco, P., Rappoport, S., et al. 1998, ApJ, 496, L5
- Urdampilleta, I., Akamatsu, H., Mernier, F., et al. 2018, A&A, 618, A74
- Urdampilleta, I., Simionescu, A., Kaastra, J. S., et al. 2021, A&A, 646, A95
- Vacca, V., Feretti, L., Giovannini, G., et al. 2014, A&A, 561, A52
- van der Velden, E. 2020, J. Open Source Softw., 5, 2004
- van Weeren, R. J., Brunetti, G., Brügggen, M., et al. 2016, ApJ, 818, 204
- van Weeren, R. J., de Gasperin, F., Akamatsu, H., et al. 2019, Space Sci. Rev., 215, 16
- Vikhlinin, A., Markevitch, M., & Murray, S. S. 2001, ApJ, 551, 160
- Walker, S. A., Hlavacek-Larrondo, J., Gendron-Marsolaïs, M.-L., et al. 2017, MNRAS, 468, 2506
- Walker, S. A., Sanders, J. S., & Fabian, A. C. 2016, MNRAS, 461, 684
- Walker, S. A., Zuhone, J. A., Fabian, A. C., & Sanders, J. S. 2018, Nature Astron., 2, 292
- Wang, Q. H., Giacintucci, S., & Markevitch, M. 2018, ApJ, 856, 162
- Wang, Q. H., Markevitch, M., & Giacintucci, S. 2016, ApJ, 833, 99

Appendix A: Additional images of the Bullet Cluster

In Fig. A.1 we collect the MeerKAT images of the Bullet Cluster filtered with the edge-detection methods outlined in Section 3.

In Fig. A.2 we show the temperature error map corresponding to Fig. 6.

In Fig. A.3 we report the residuals obtained by subtracting the best-fit exponential models (circular, elliptical, and skewed) describing the surface brightness profile of the radio halo in the Bullet Cluster derived with the Halo-Flux Density Calculator (HALO-FDCA; Boxelaar et al. 2021) from the MeerKAT image. Deviations from these smooth models are due to substructures (such as edges) which are highlighted in the residual maps.

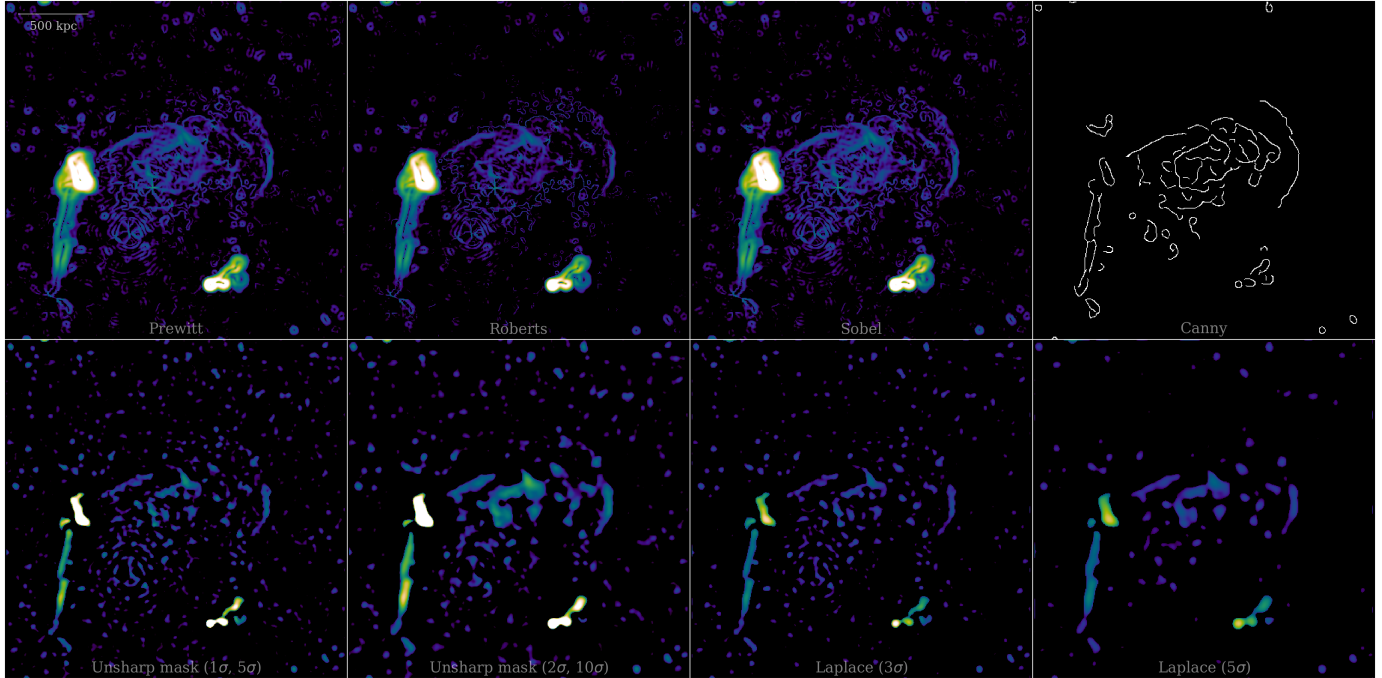


Fig. A.1. Different edge-detection algorithms (see labels) applied to the MeerKAT image of the Bullet Cluster.

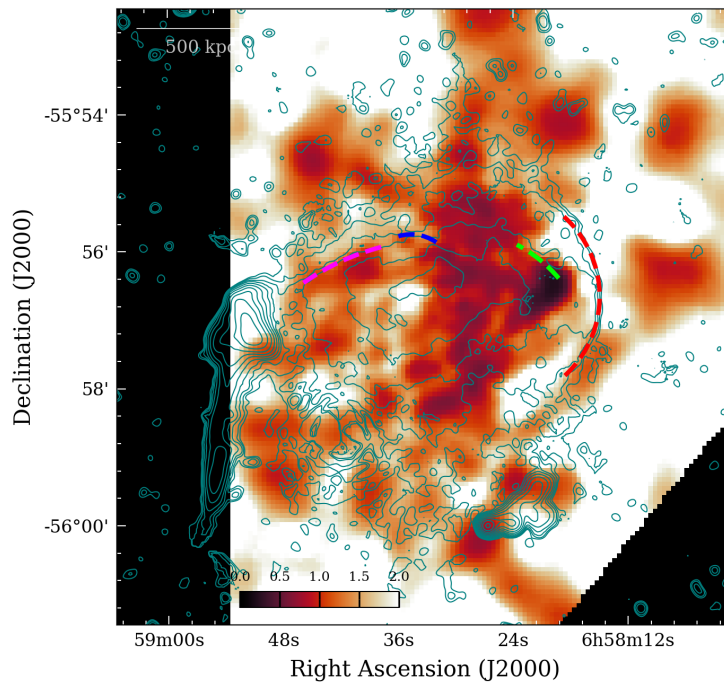


Fig. A.2. Temperature error map of the Bullet cluster (cf. with Fig. 6).

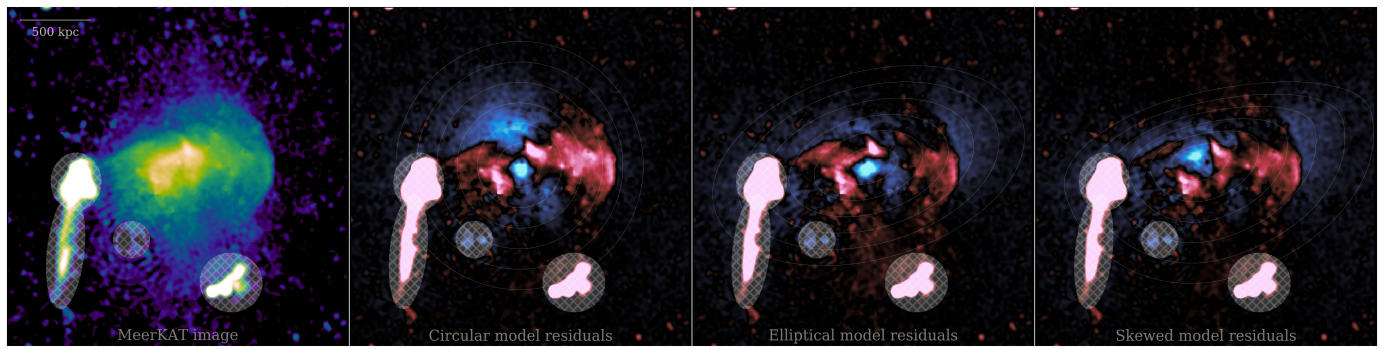


Fig. A.3. MeerKAT image of the Bullet Cluster and residuals of the best-fit exponential models (red is positive, blue is negative). Isocontour levels of the corresponding model are reported. Hatched regions were masked during the fit with HALO-FDCA.

Appendix B: Radio halos in MGCLS with radio surface brightness gradients

Abell 85 The surface brightness drops at the boundary of the radio halo emission. This edge is coincident with a cold front observed in the X-rays (Ichinohe et al. 2015; Rahaman et al. 2022).

Abell 209 The surface brightness gradient is detected at the boundary of the diffuse emission.

Abell 521 A mild gradient located in a low surface brightness region is found at the northern border of the radio halo. Deeper data will help to determine the significance of this jump.

Abell 2744 Multiple radio gradients are identified in the radio halo. The southeastern edge (green color) is located in a region where a shock front has been detected with X-ray observations (Owers et al. 2011; Jauzac et al. 2016).

Abell 3562 A possible gradient is observed in a region where the radio halo has low surface brightness; confirmation will require deeper observations.

MACS J0417.5-1155 Two radio edges co-located with two cold fronts observed in the X-rays (Botteon et al. 2018; Pandge et al. 2019) are detected.

RXC J1314.4-2525 Two gradients are observed at the boundary of the radio halo.

J0225.9-4154 (Abell 3017) Two surface brightness gradients are identified. The southern jump is located in the direction where a cold front and a shock front have been detected in X-rays (Chon et al. 2019).

J0232.2-4420 (PSZ2 G259.98-63.43) A surface brightness gradient is present in the northern region of the radio halo. The subtraction of the bright AGN at the center of the diffuse emission introduced some artifacts in the image that were avoided during the extraction of the surface brightness profile.

J0638.7-5358 (Abell S592) A significant surface brightness jump is found in coincidence with an X-ray-detected shock front (Botteon et al. 2018).

J0645.4-5413 (Abell 3404) The gradient in the inner region of the cluster is mild and a better characterization will require deeper observations.

J2023.4-5535 (PSZ1 G342.33-34.92) The radio edge is located at the eastern boundary of the radio halo.

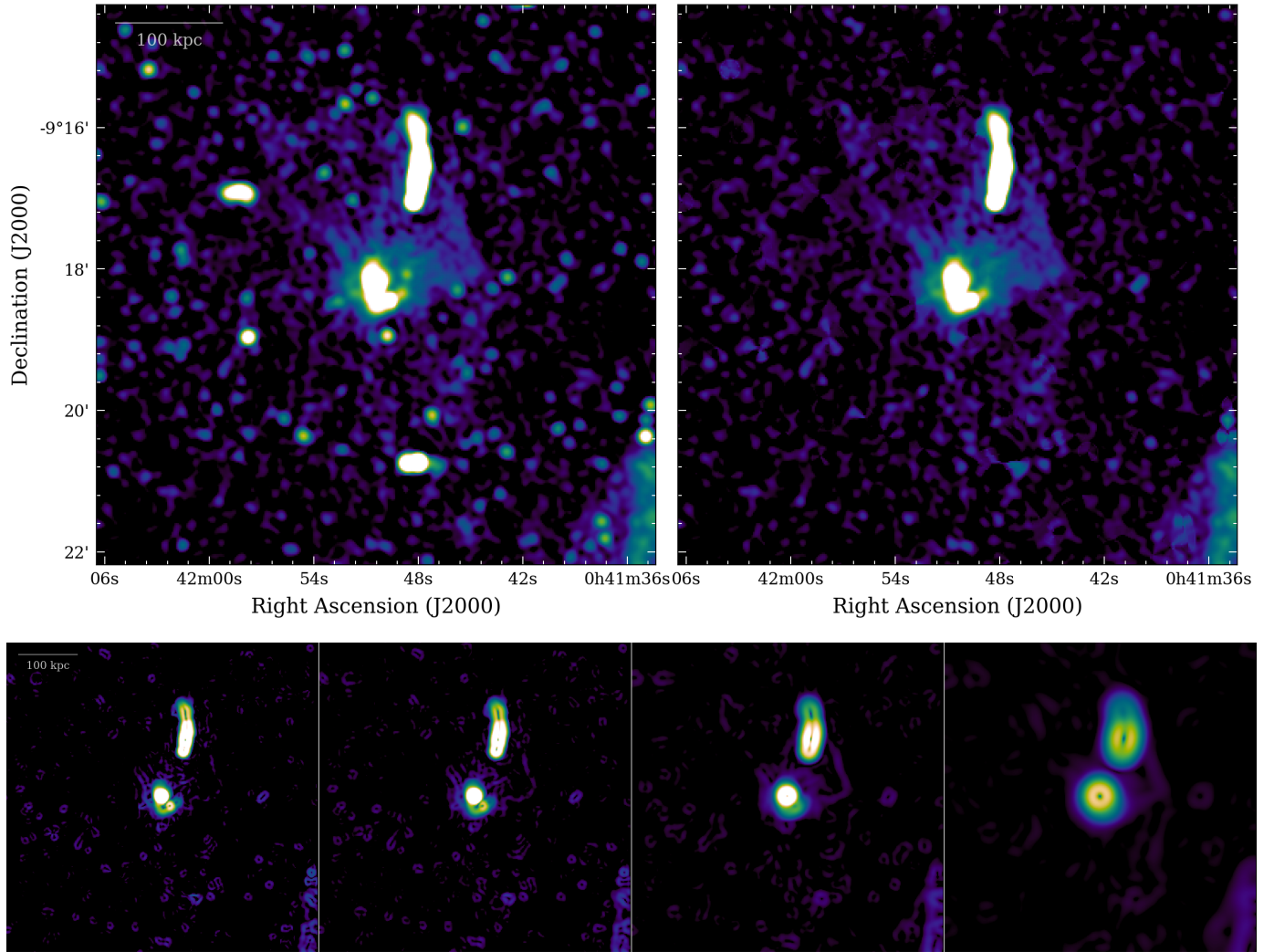


Fig. B.1. Same as Fig. 1 but for Abell 85.

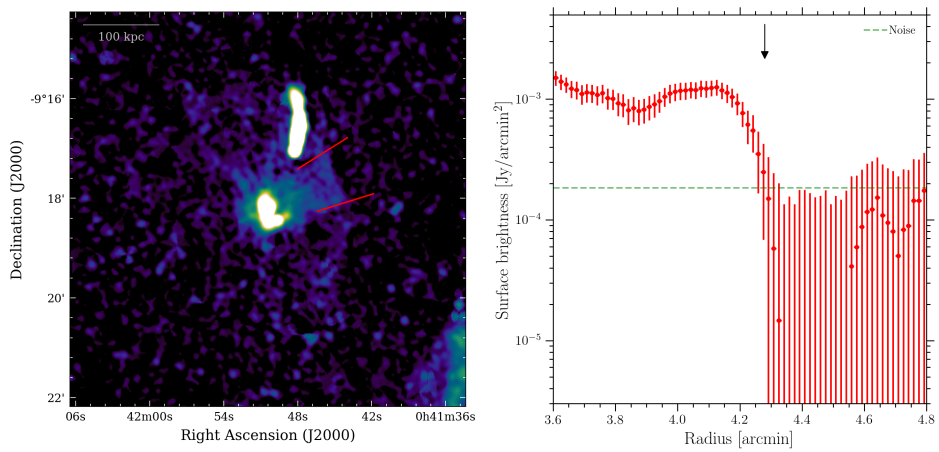


Fig. B.2. Same as Fig. 3 but for Abell 85.

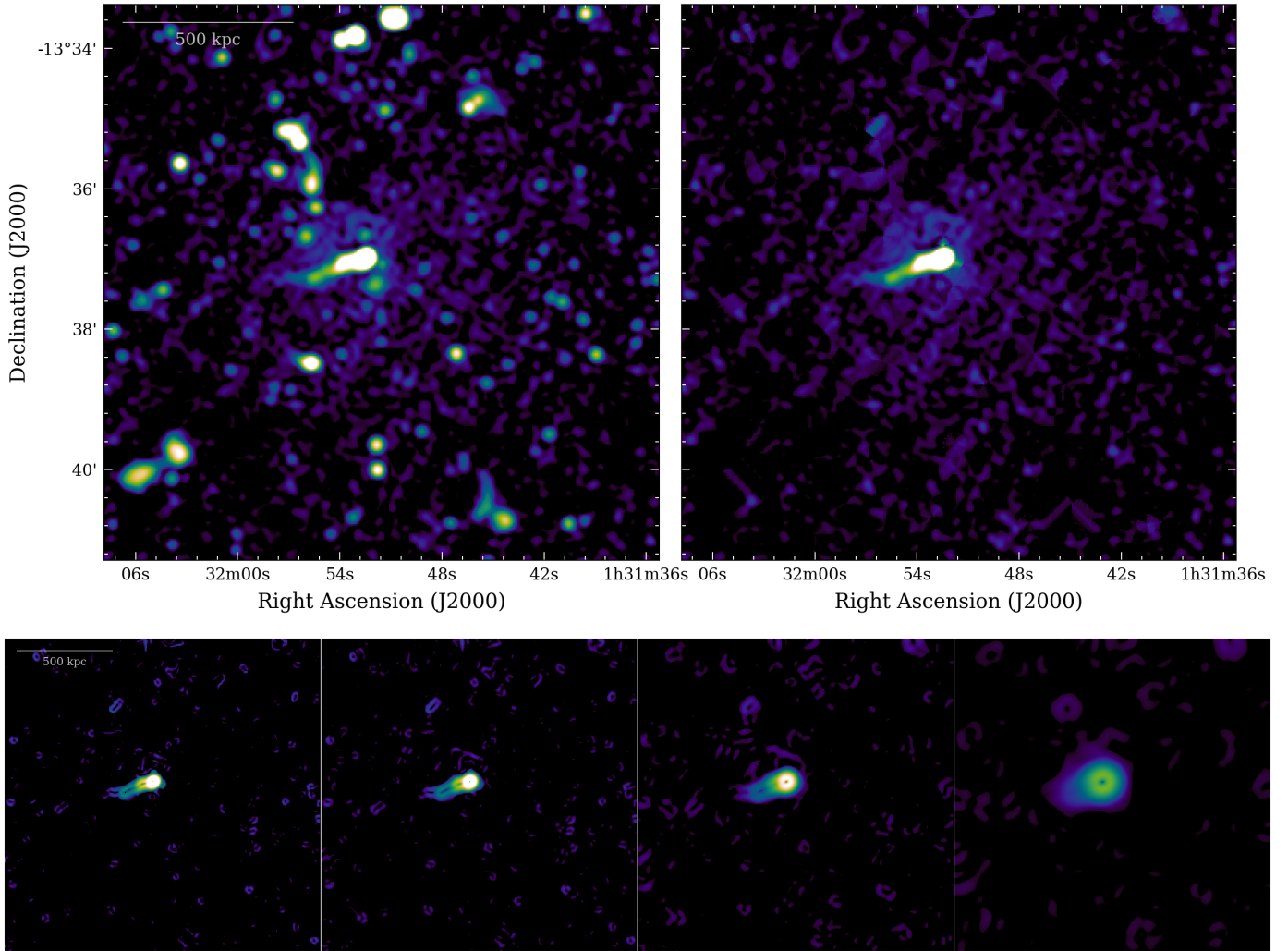


Fig. B.3. Same as Fig. 1 but for Abell 209.

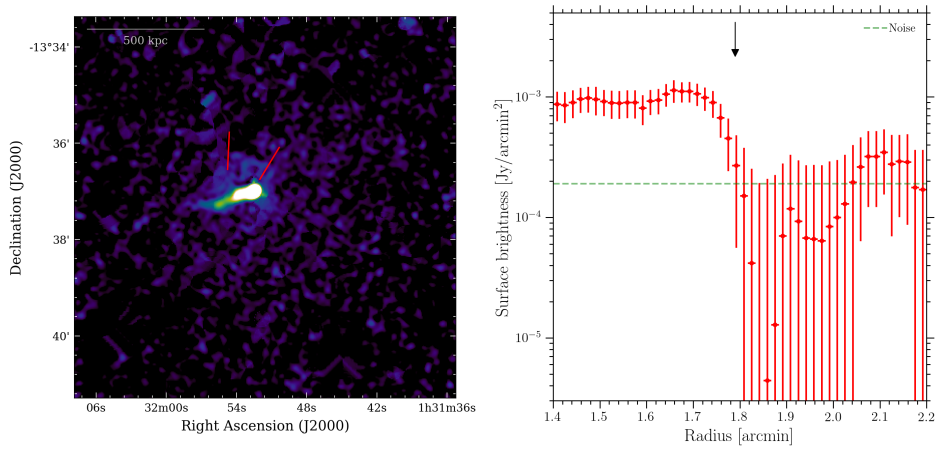


Fig. B.4. Same as Fig. 3 but for Abell 209.

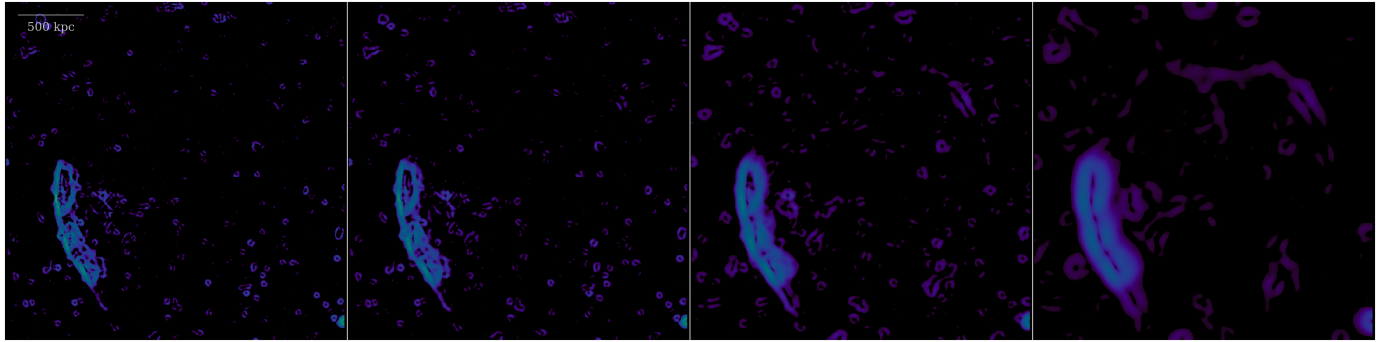
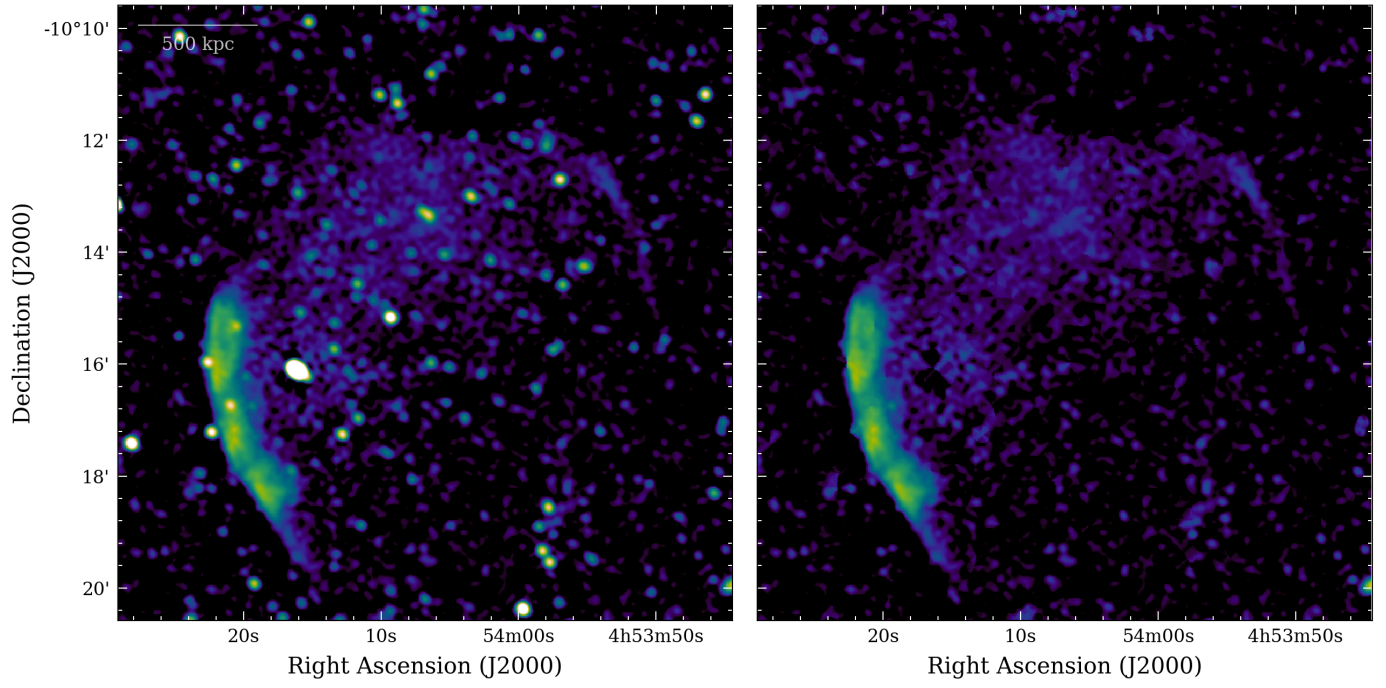


Fig. B.5. Same as Fig. 1 but for Abell 521.

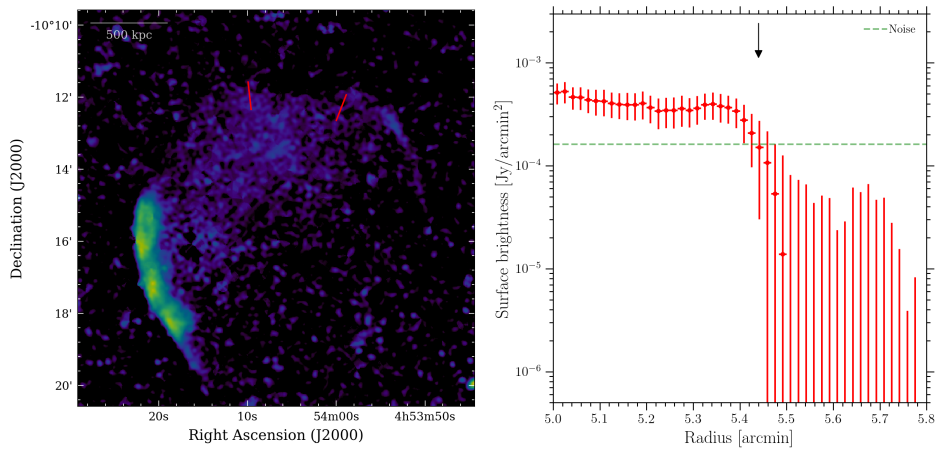


Fig. B.6. Same as Fig. 3 but for Abell 521.

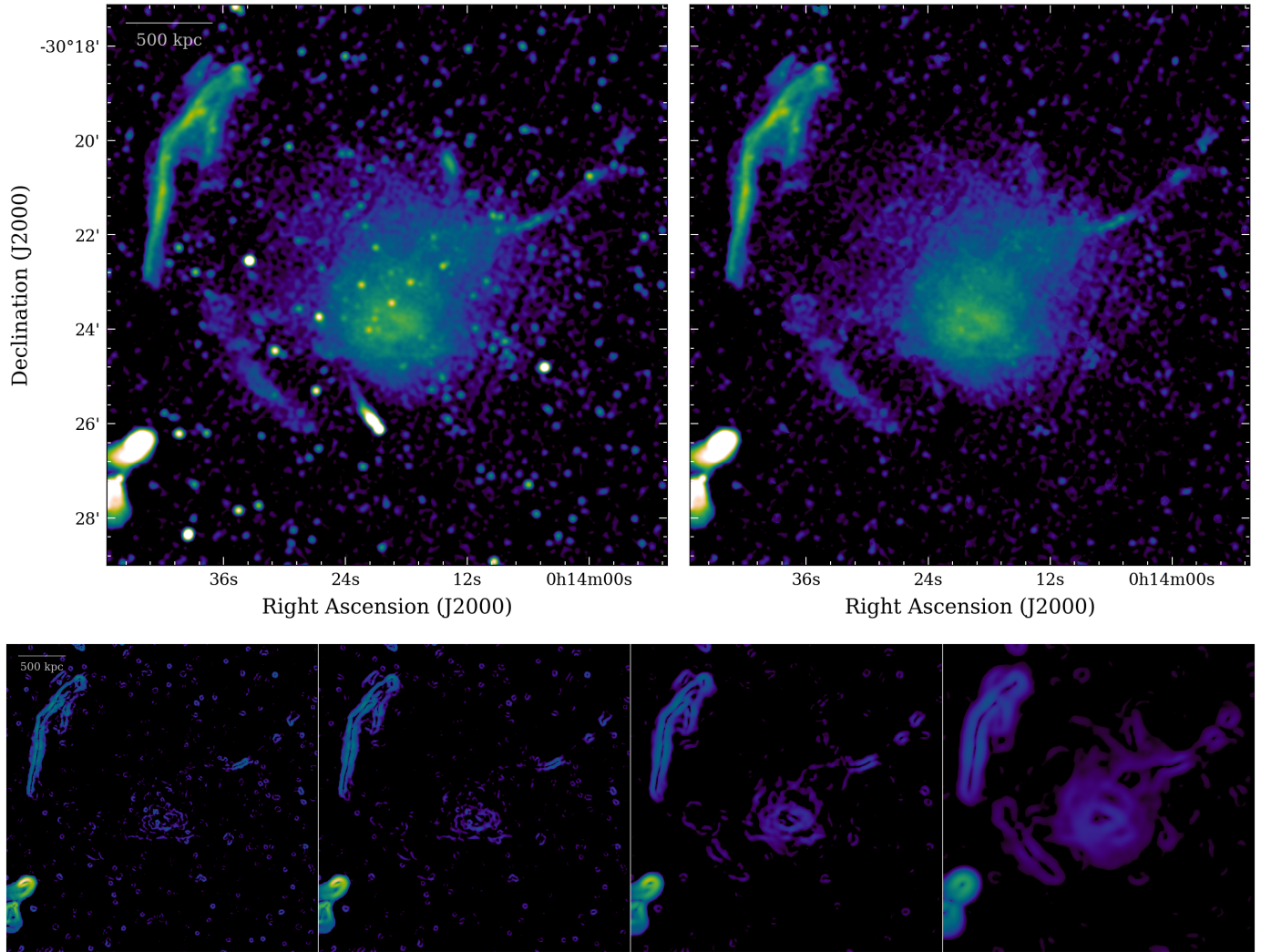


Fig. B.7. Same as Fig. 1 but for Abell 2744.

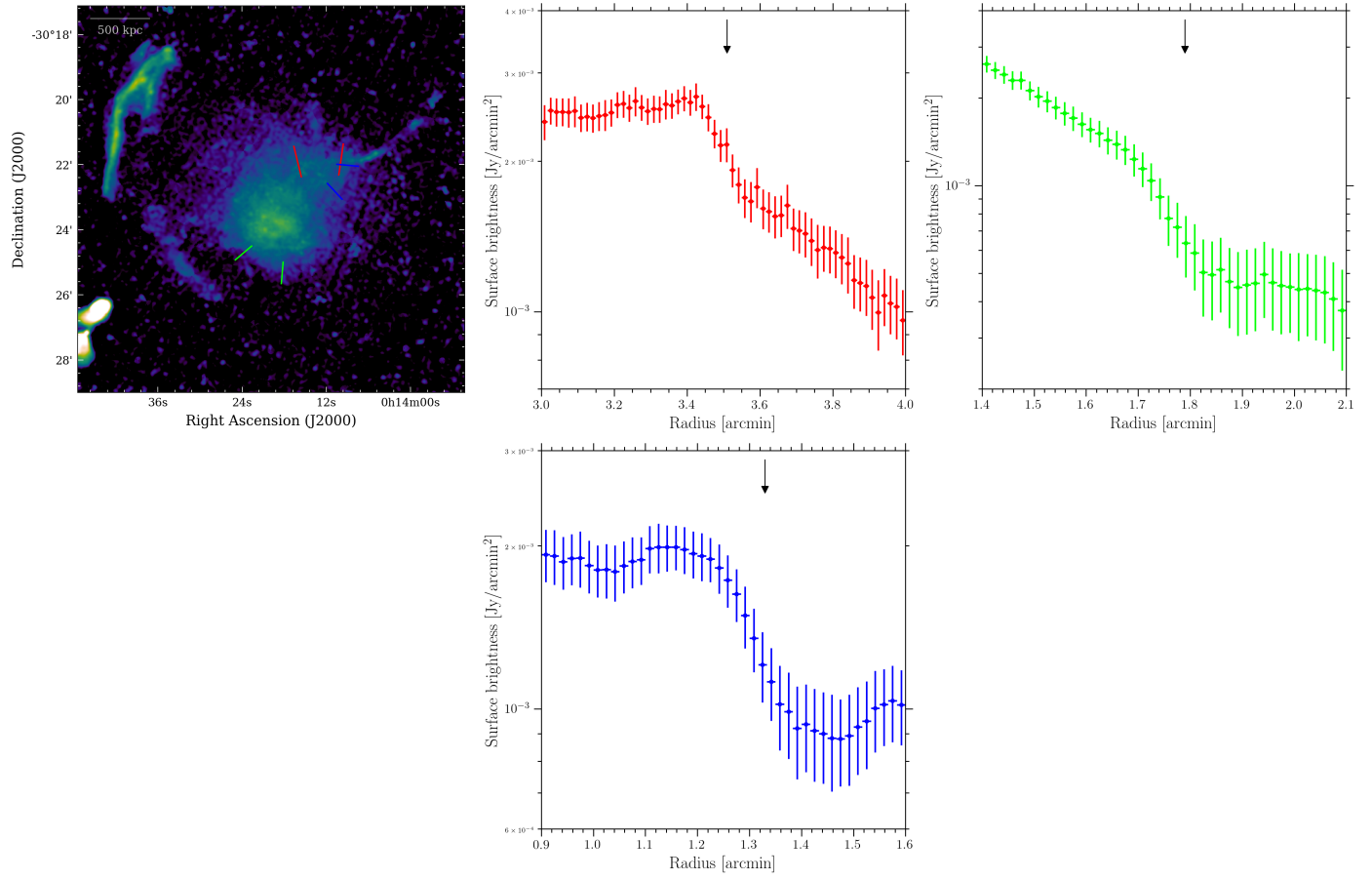


Fig. B.8. Same as Fig. 3 but for Abell 2744.

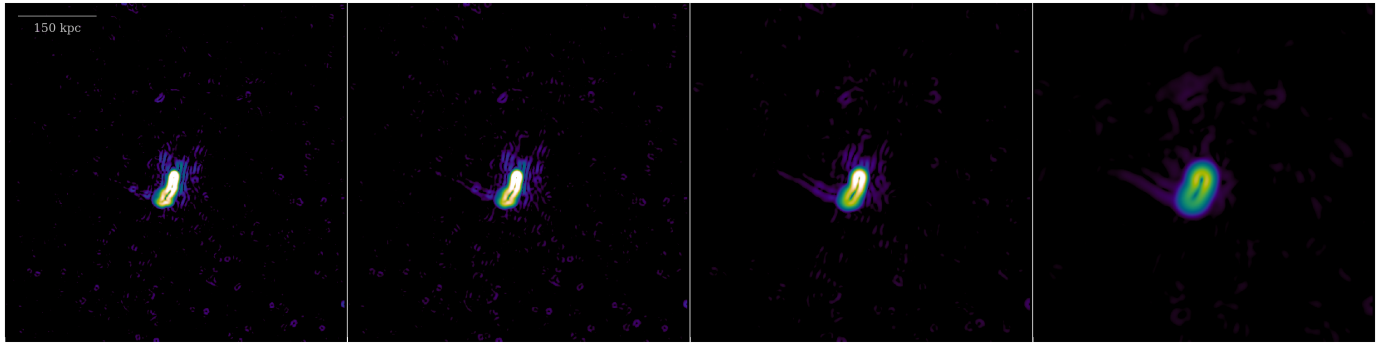
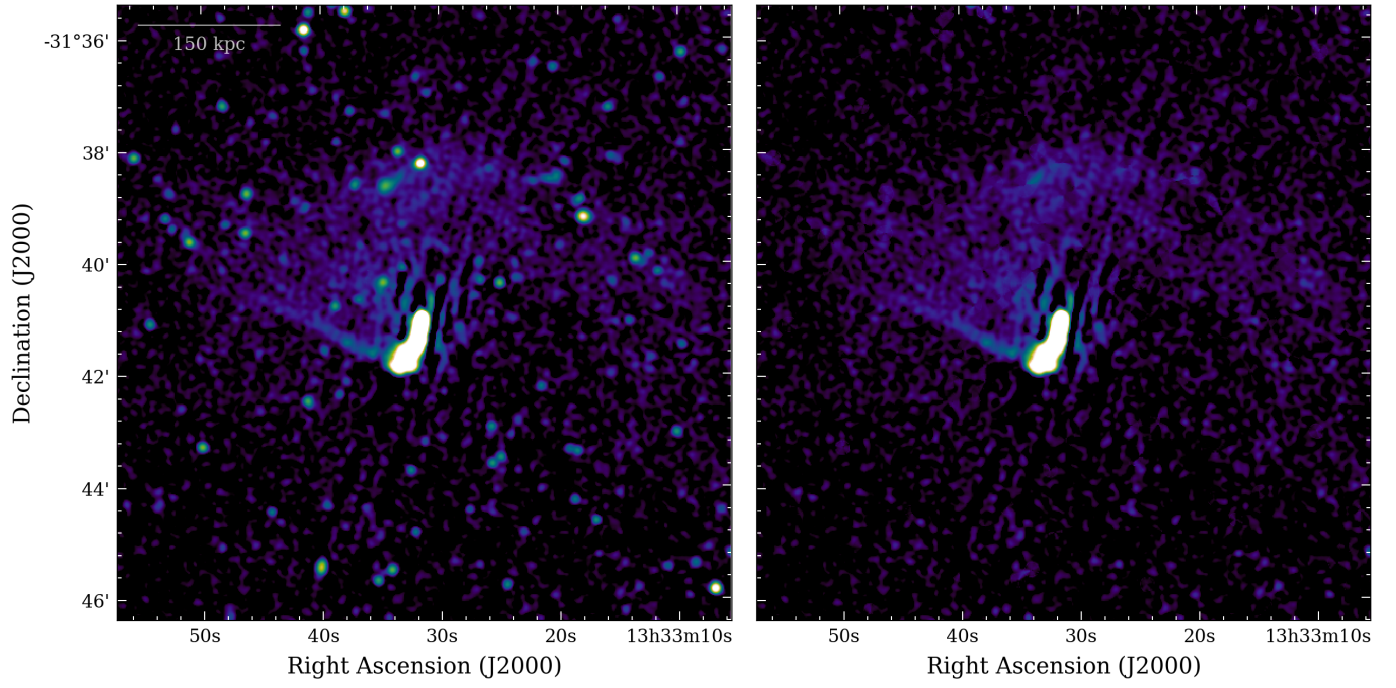


Fig. B.9. Same as Fig. 1 but for Abell 3562.

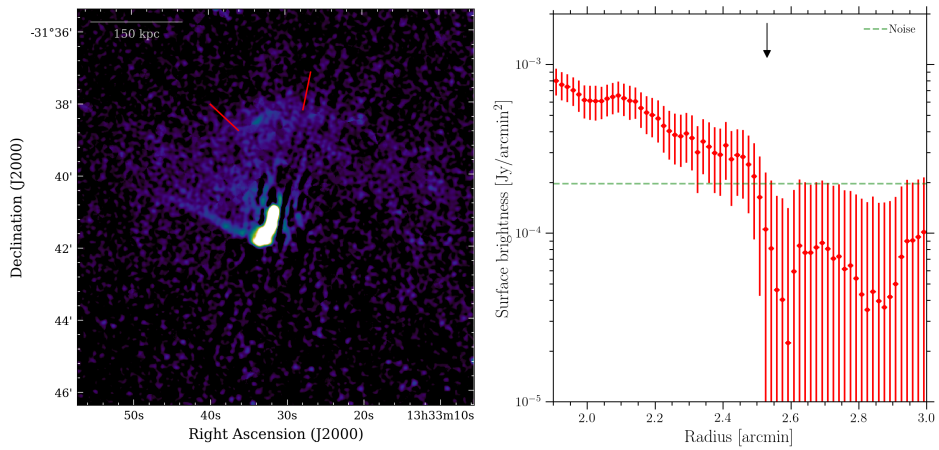


Fig. B.10. Same as Fig. 3 but for Abell 3562.

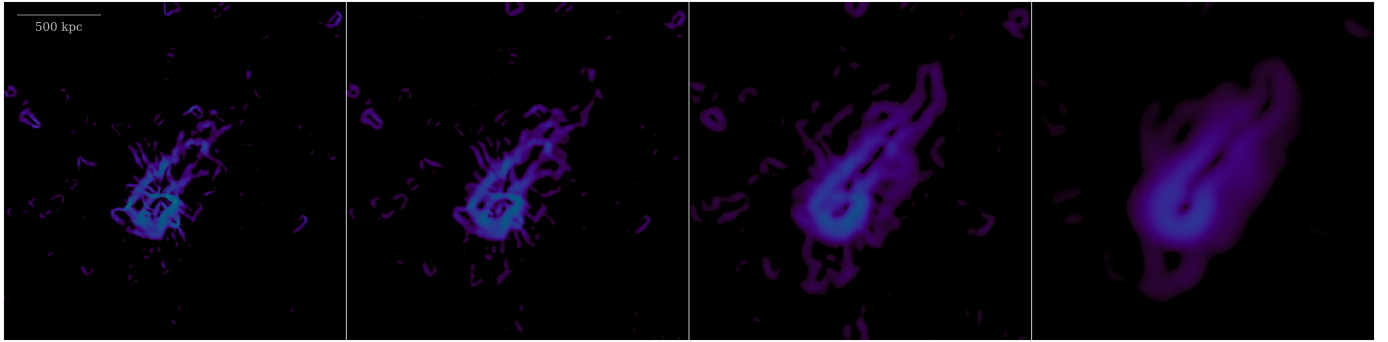
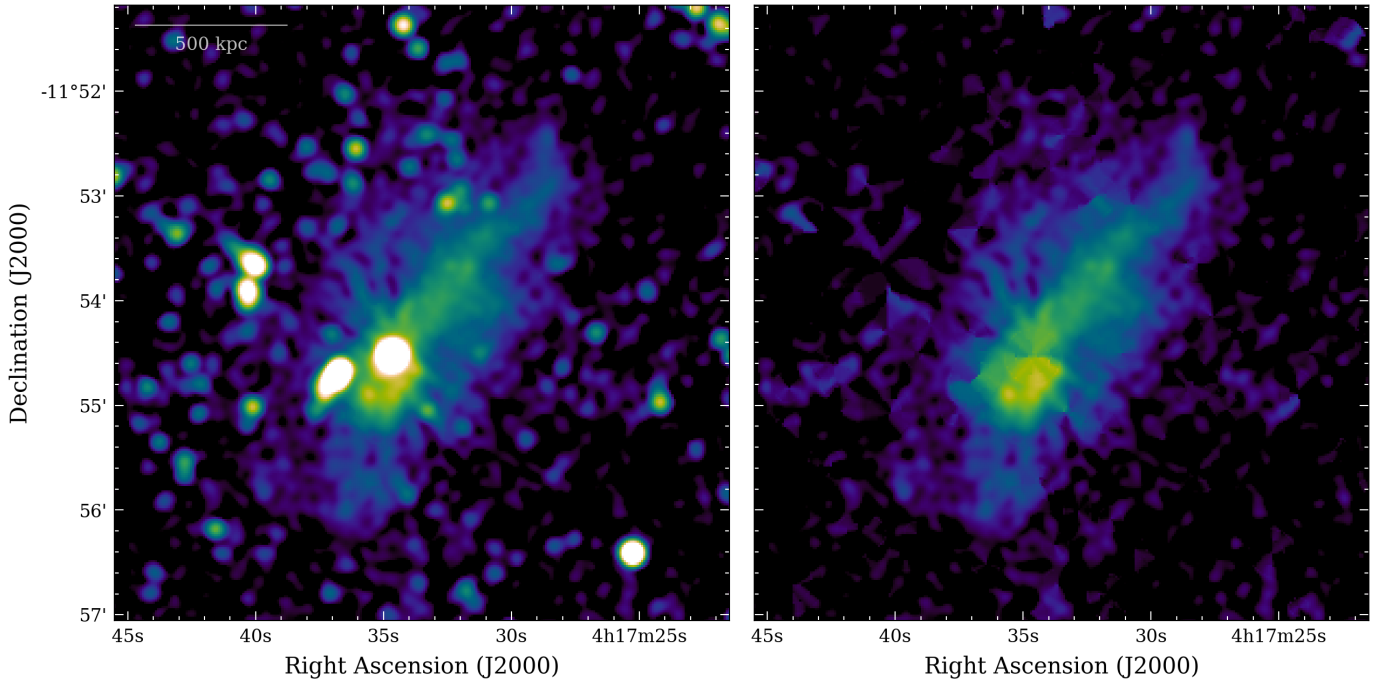


Fig. B.11. Same as Fig. 1 but for MACS J0417.5-1155.

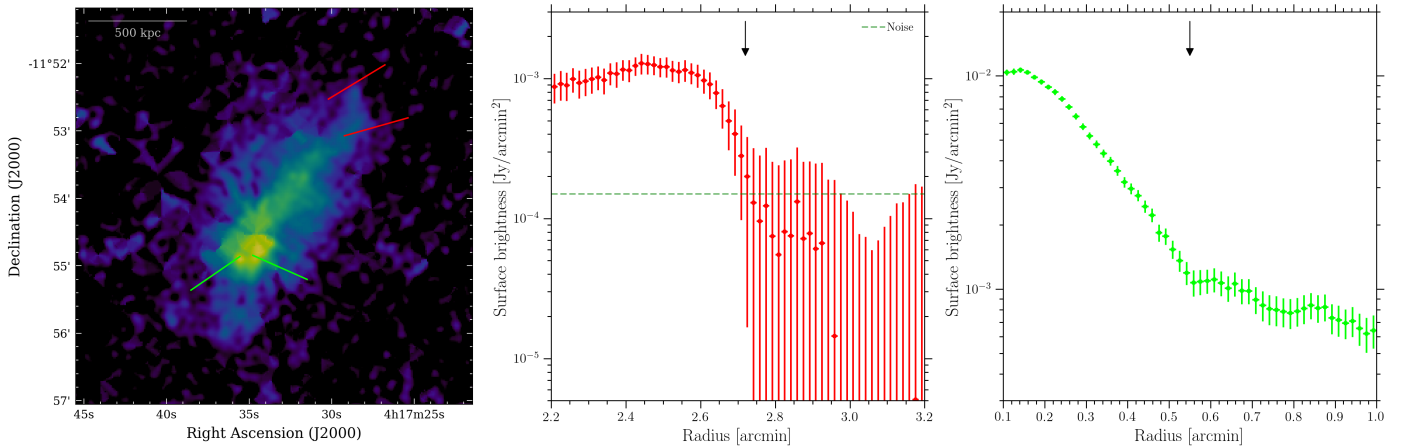


Fig. B.12. Same as Fig. 3 but for MACS J0417.5-1155.

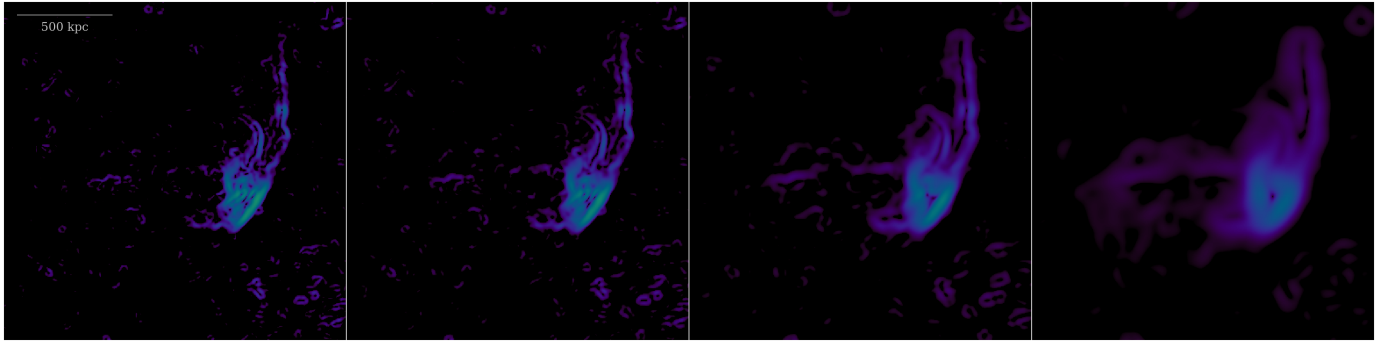
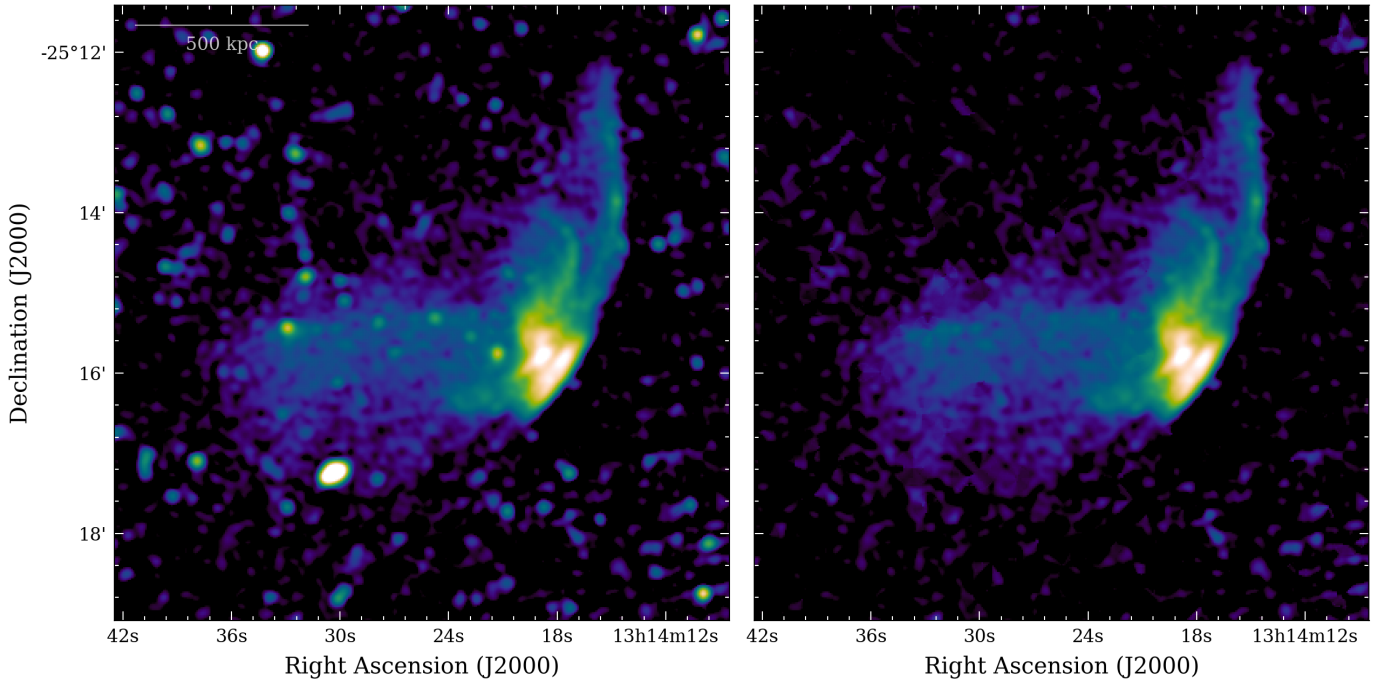


Fig. B.13. Same as Fig. 1 but for RXC J1314.4-2525.

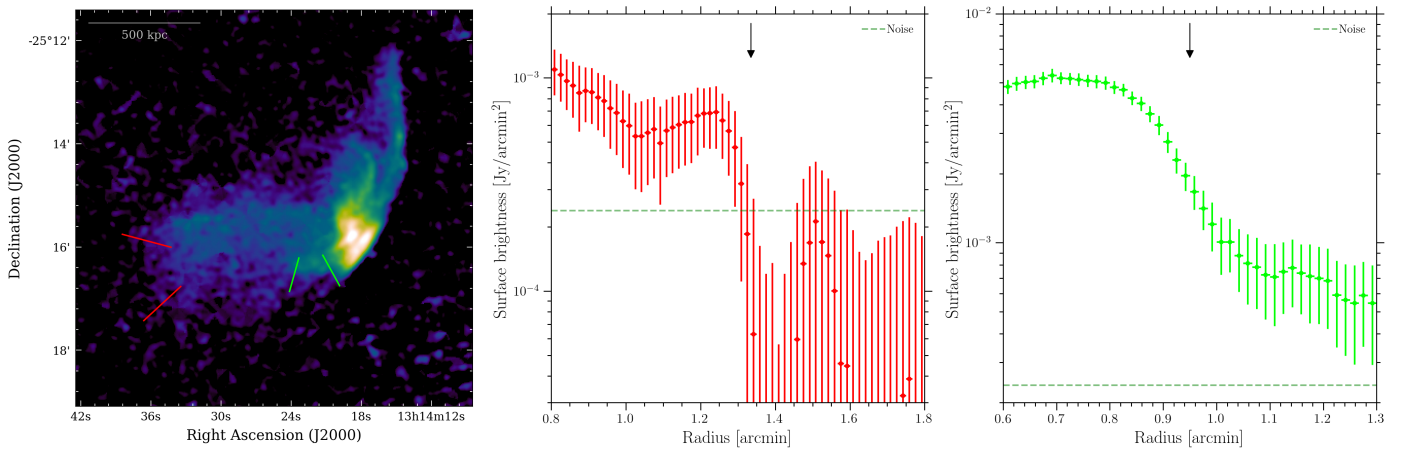


Fig. B.14. Same as Fig. 3 but for RXC J1314.4-2525.

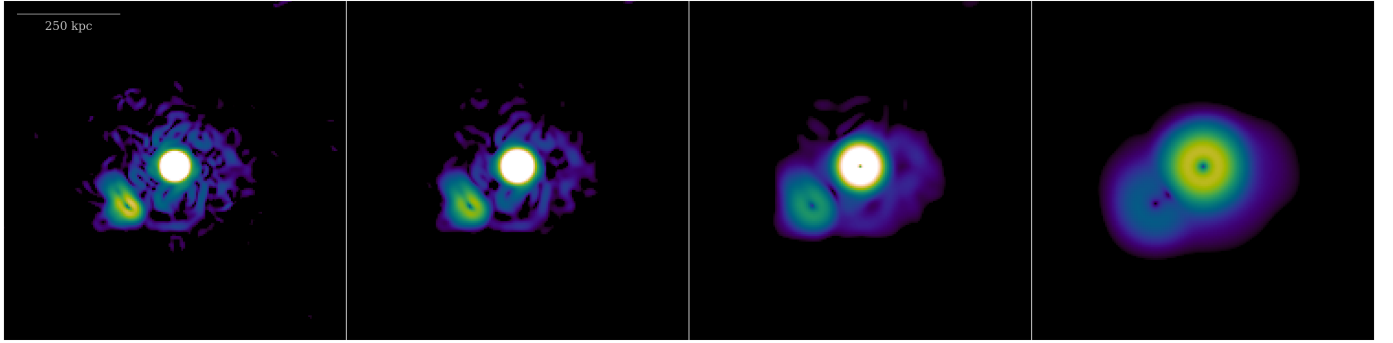
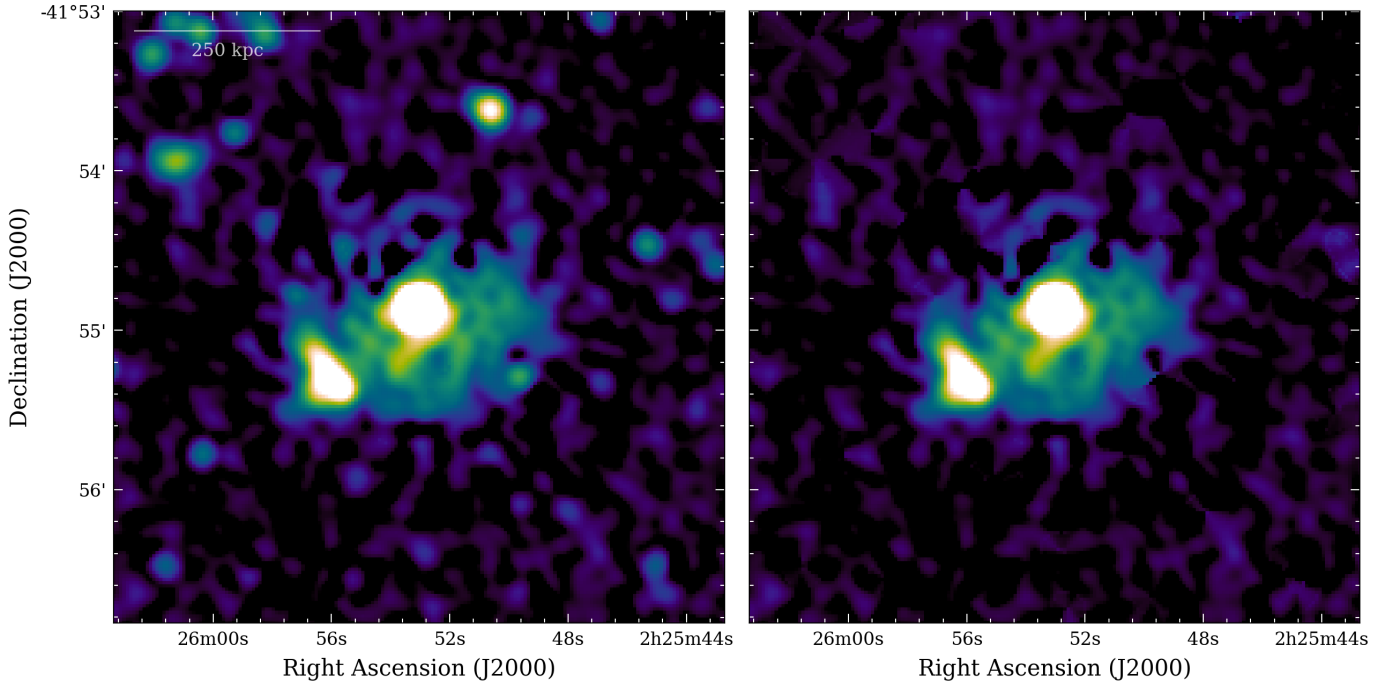


Fig. B.15. Same as Fig. 1 but for J0225.9-4154.

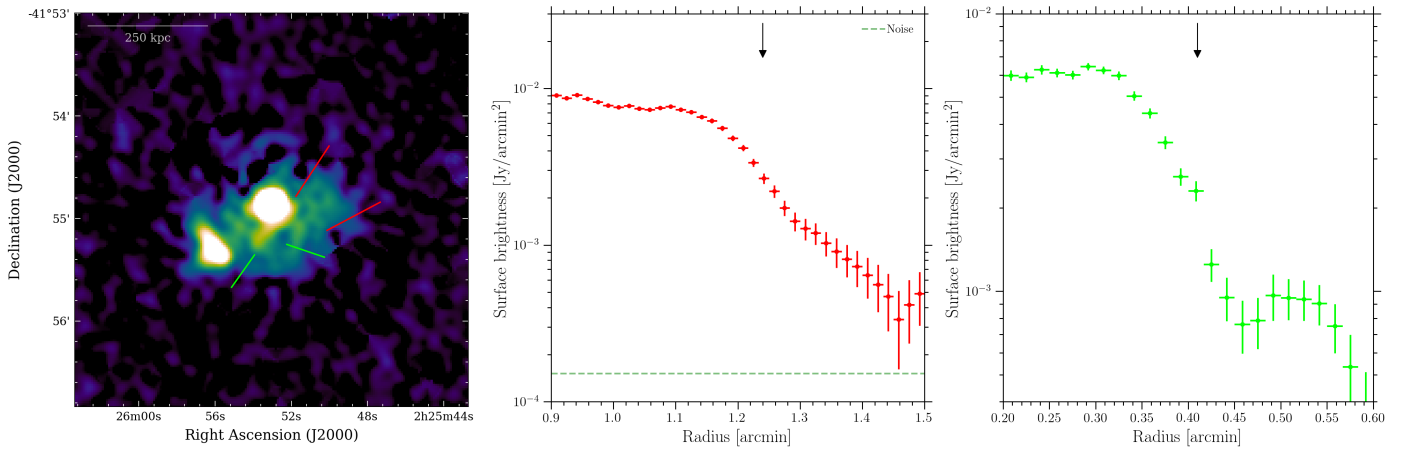


Fig. B.16. Same as Fig. 3 but for J0225.9-4154.

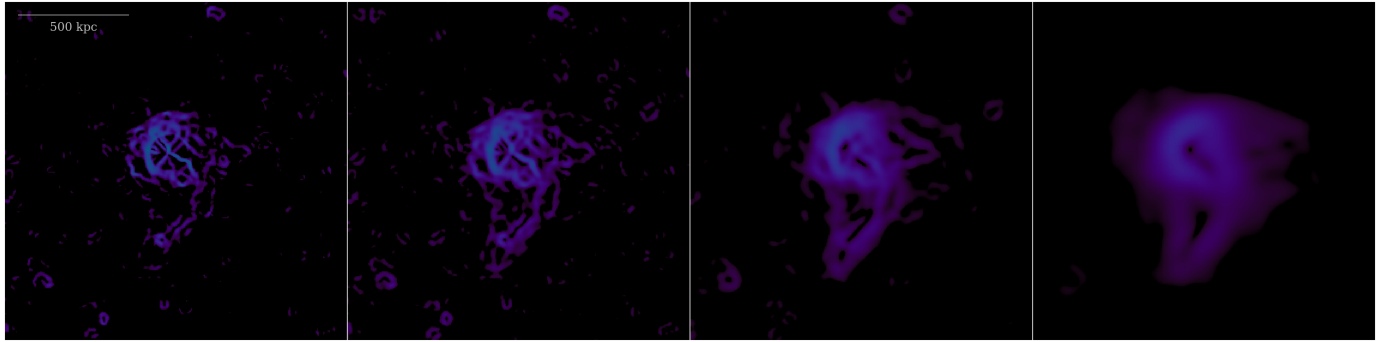
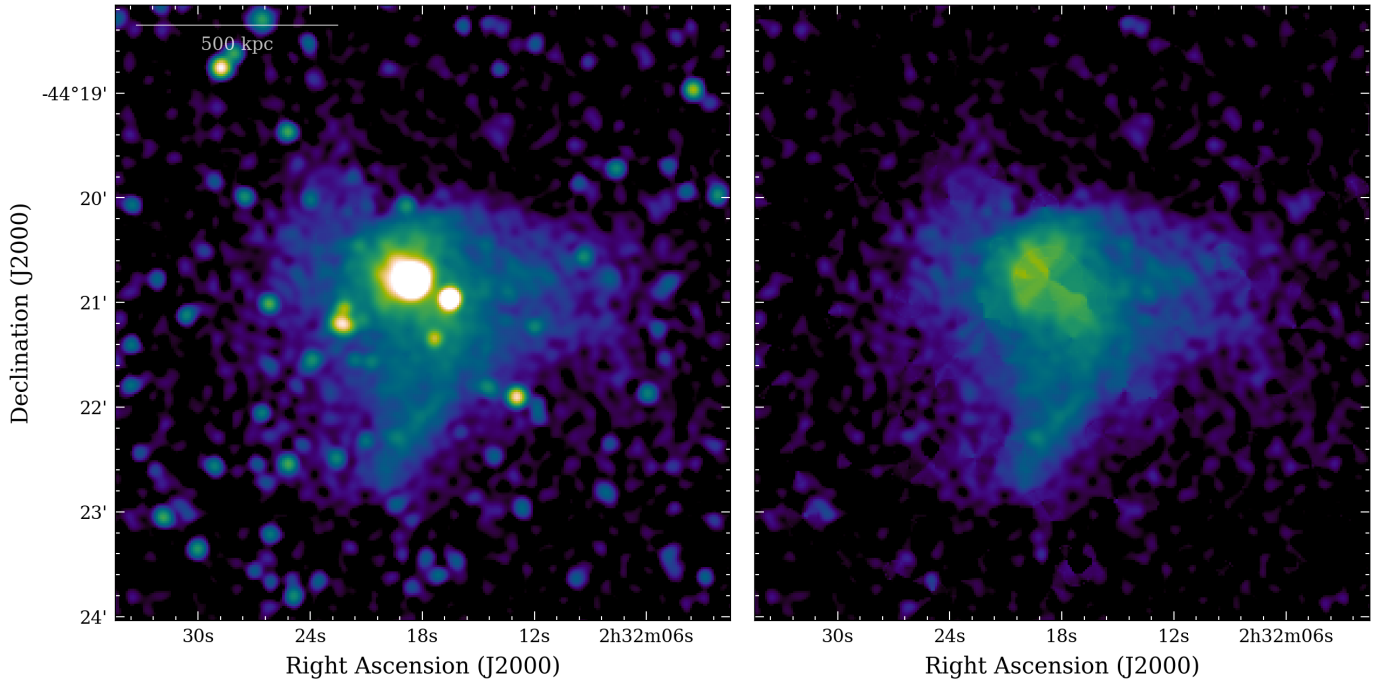


Fig. B.17. Same as Fig. 1 but for J0232.2-4420.

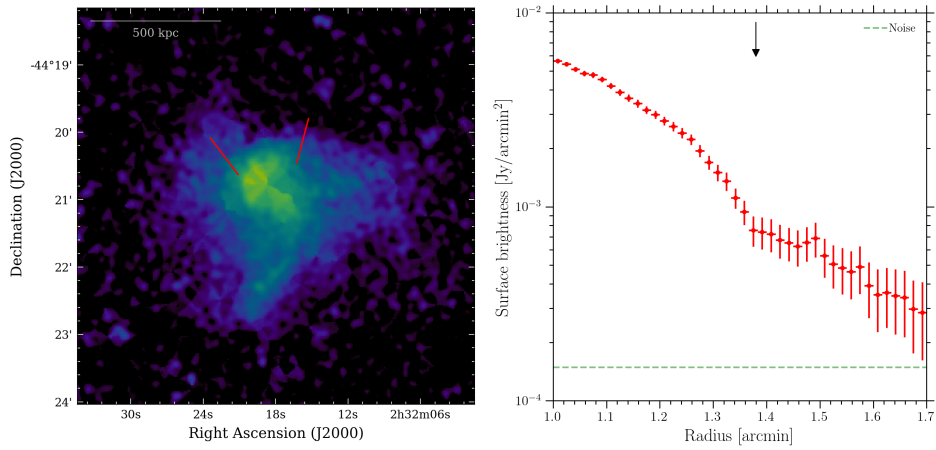


Fig. B.18. Same as Fig. 3 but for J0232.2-4420.

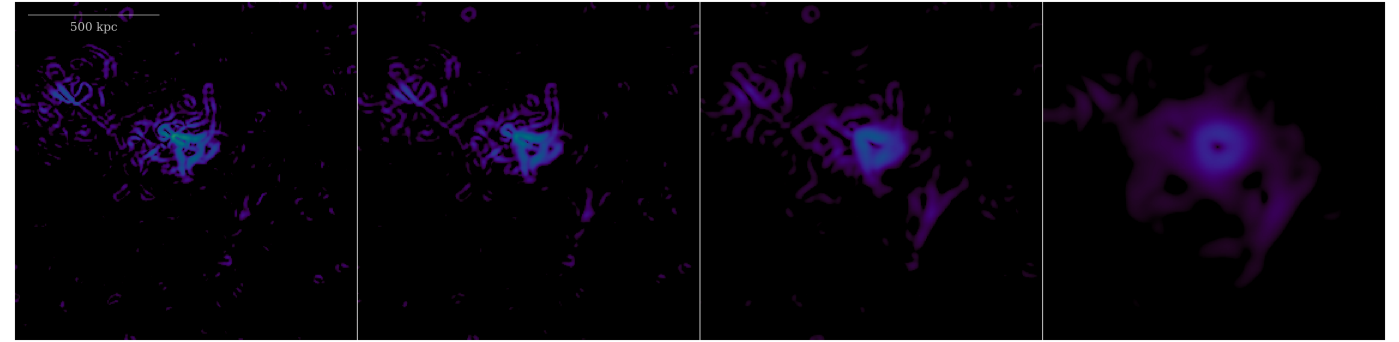
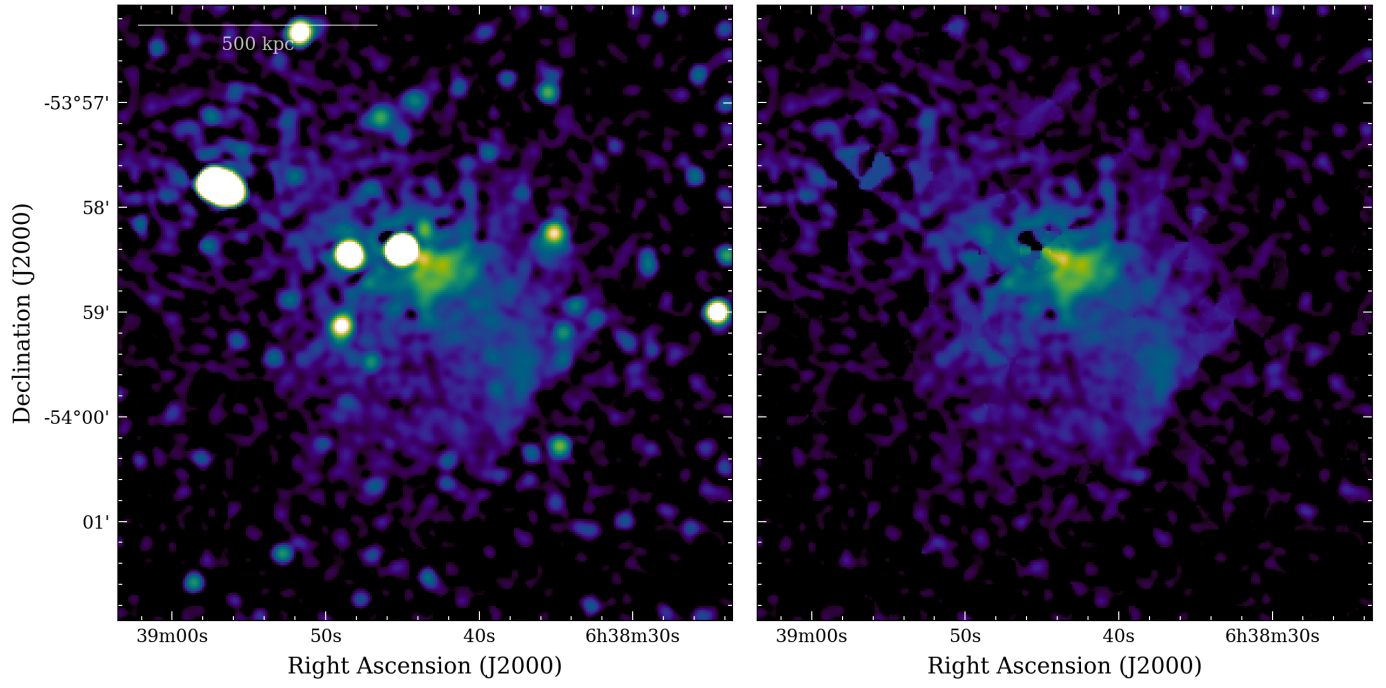


Fig. B.19. Same as Fig. 1 but for J0638.7-5358.

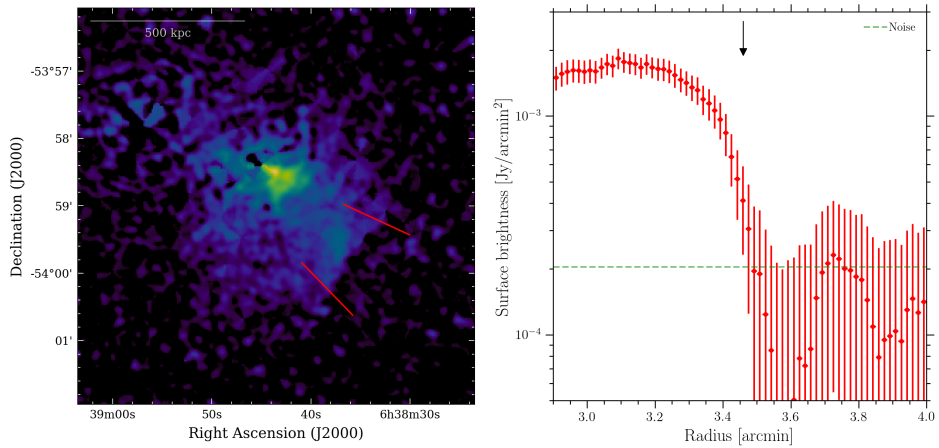


Fig. B.20. Same as Fig. 3 but for J0638.7-5358.

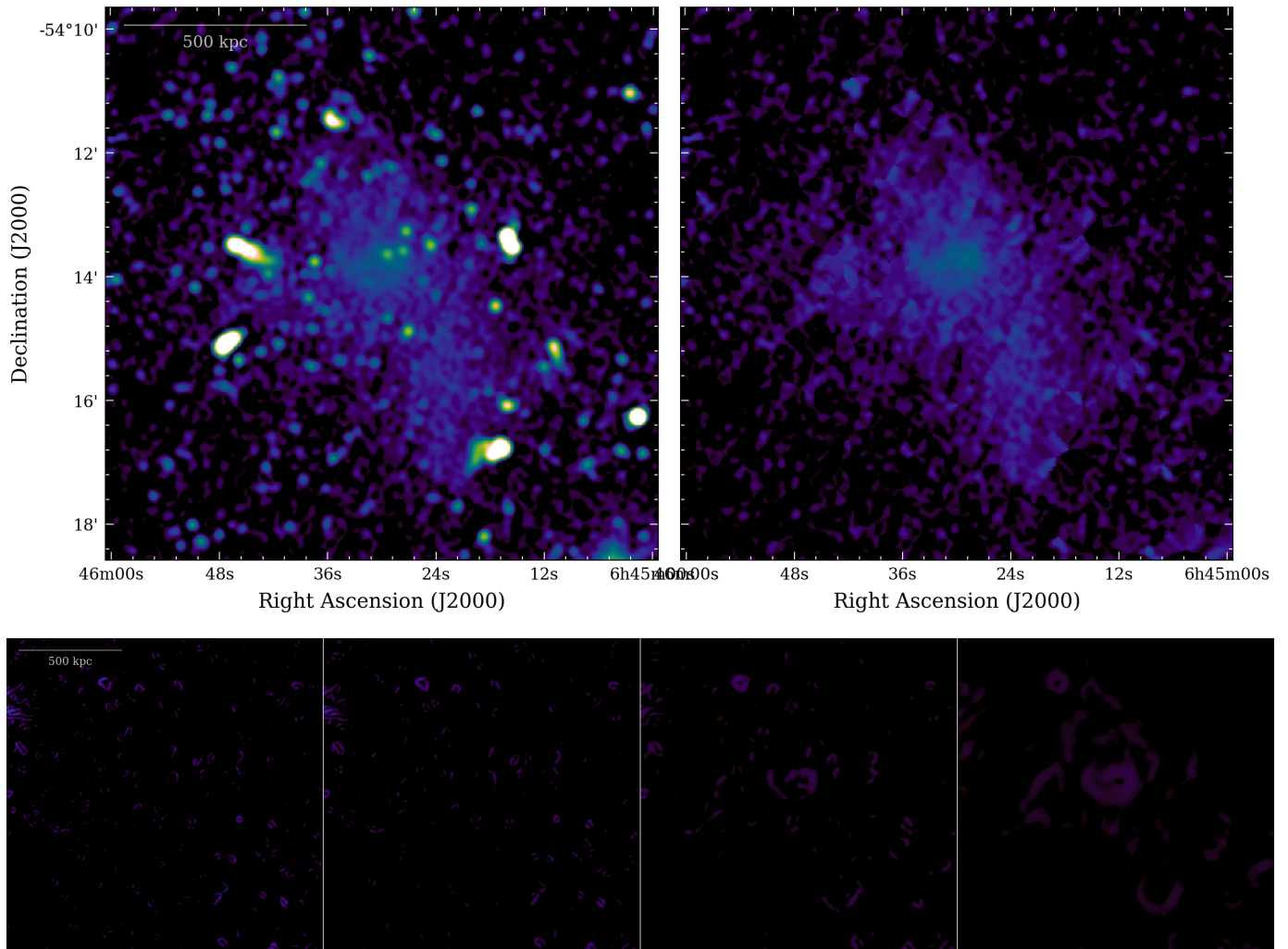


Fig. B.21. Same as Fig. 1 but for J0645.4-5413.

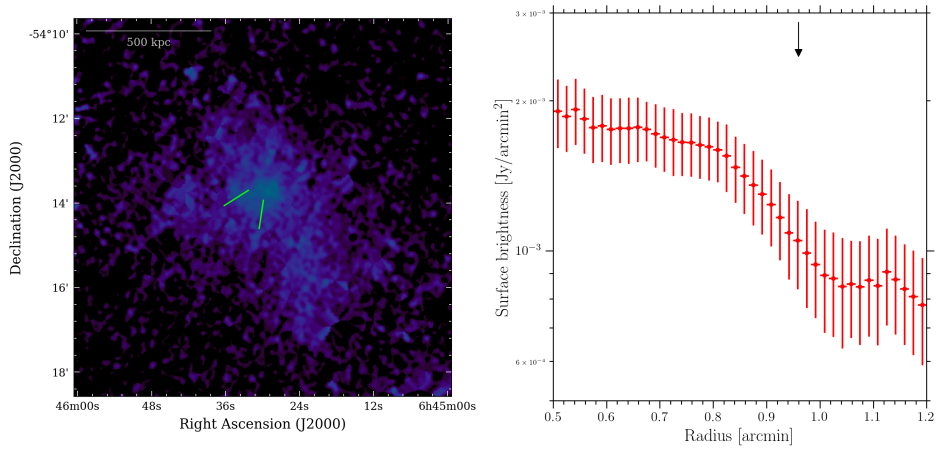


Fig. B.22. Same as Fig. 3 but for J0645.4-5413.

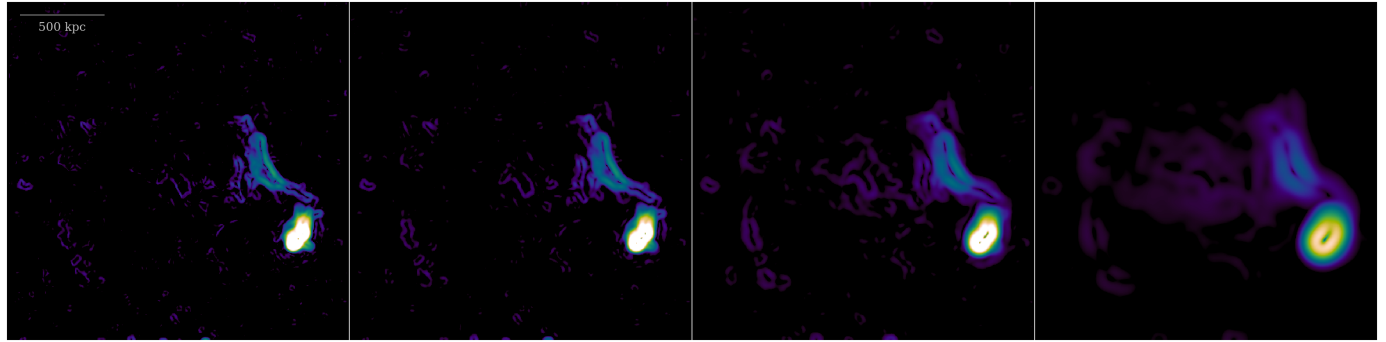
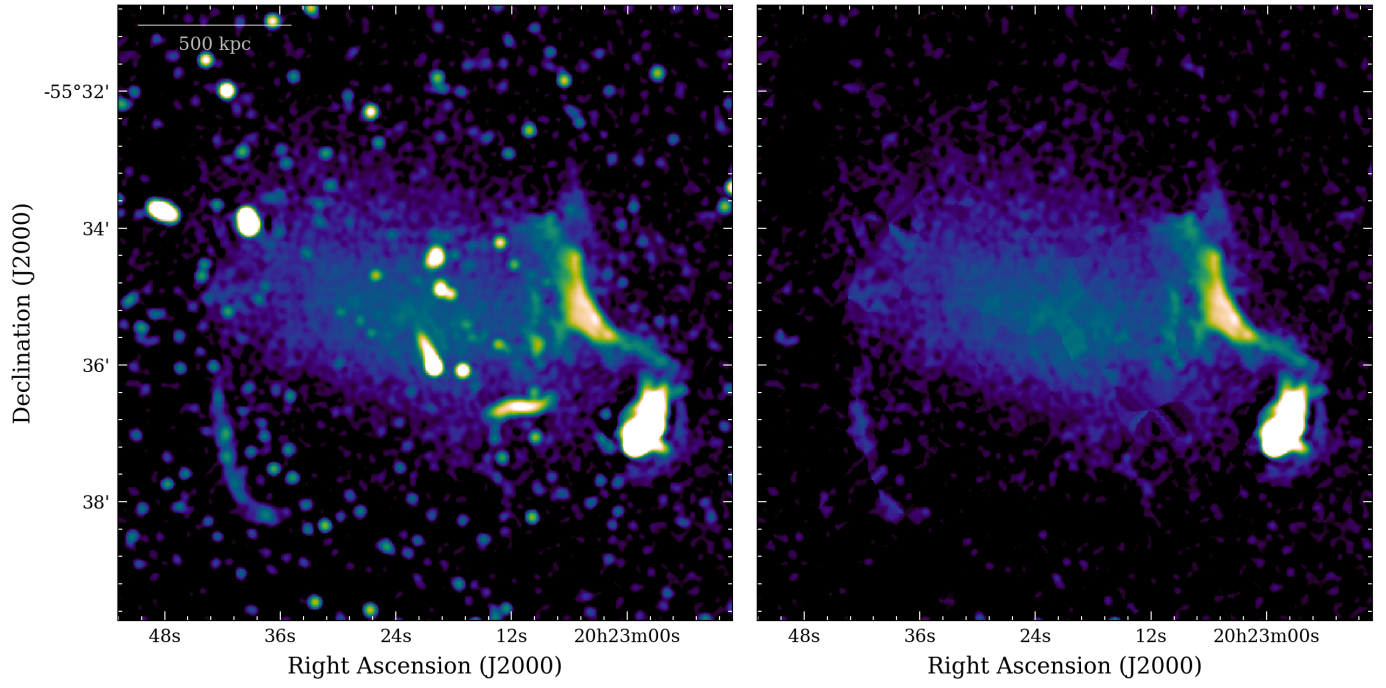


Fig. B.23. Same as Fig. 1 but for J2023.4-5535.

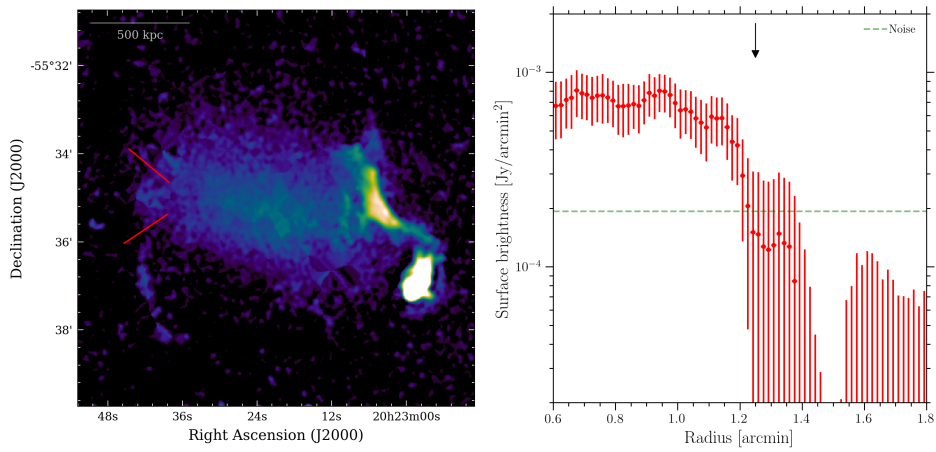


Fig. B.24. Same as Fig. 3 but for J2023.4-5535.

Appendix C: Radio halos in MGCLS without radio surface brightness gradients

The radio halos where we did not identify any radio surface brightness gradient are generally characterized by low surface brightness. In a few cases, residual calibration errors (e.g., Abell 545, Abell 3558, Abell S295) or artifacts introduced by the procedure of discrete source subtraction (e.g., Abell 2811, J0303.7-7752) are evident in the MeerKAT images.

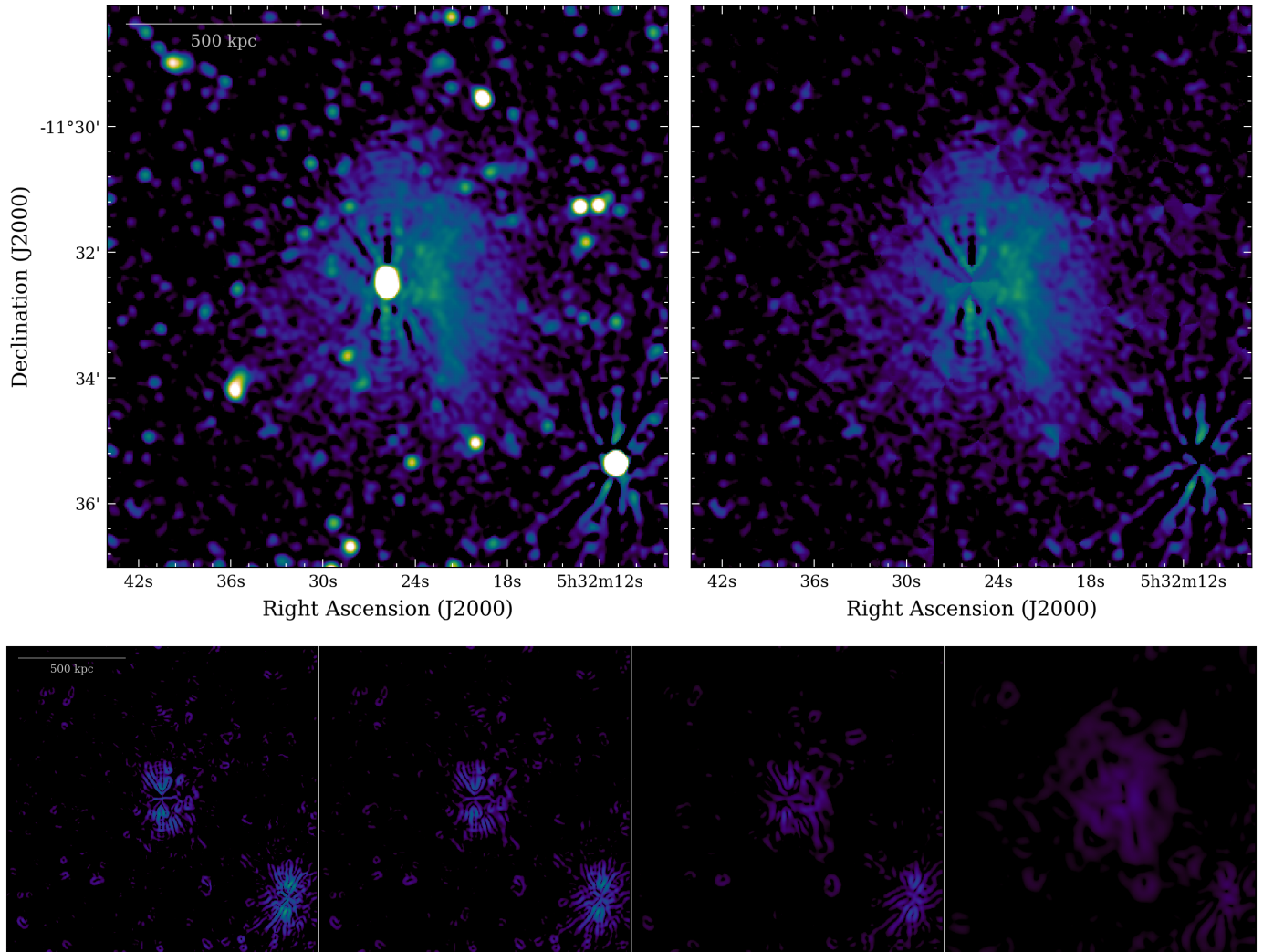


Fig. C.1. Same as Fig. 1 but for Abell 545.

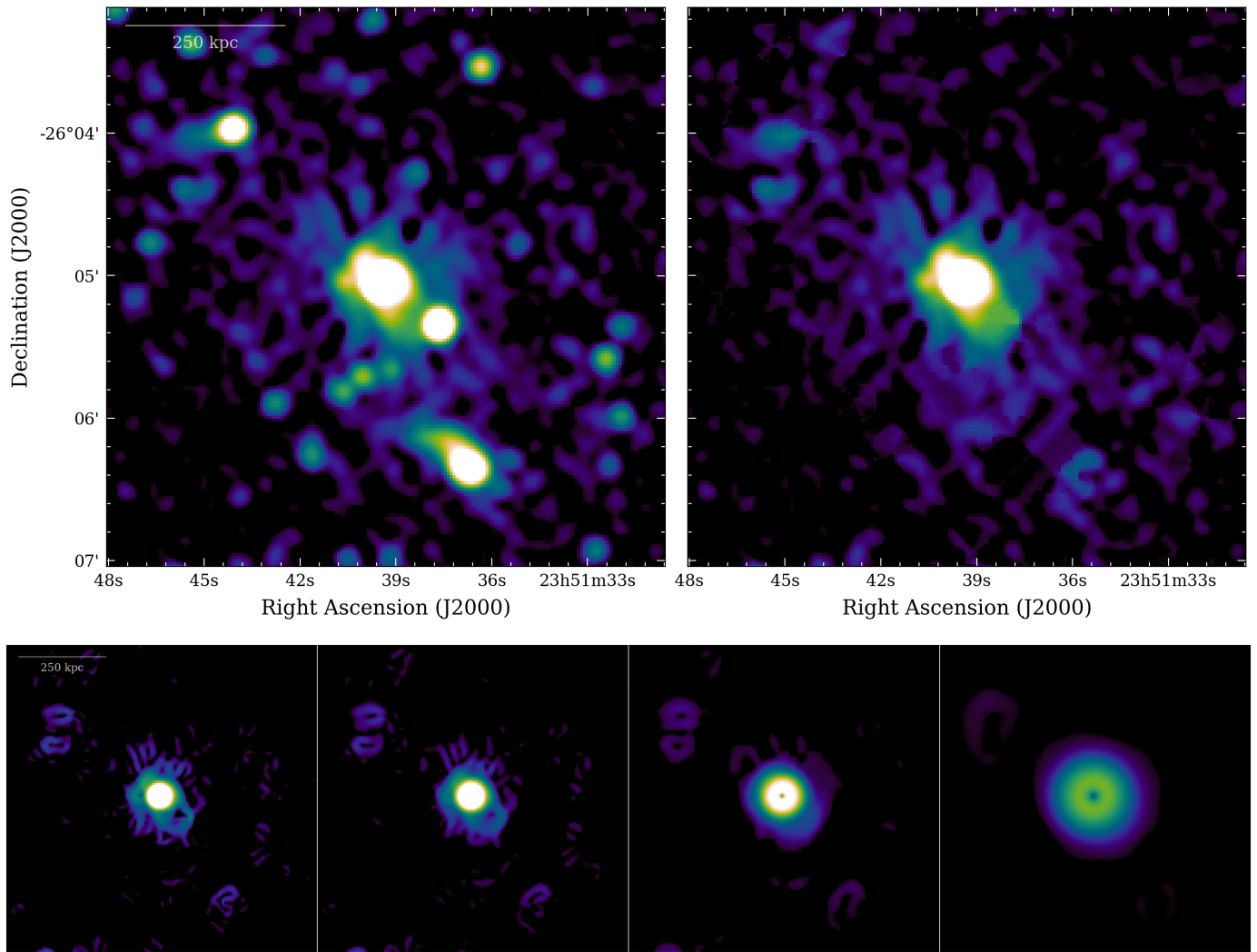


Fig. C.2. Same as Fig. 1 but for Abell 2667.

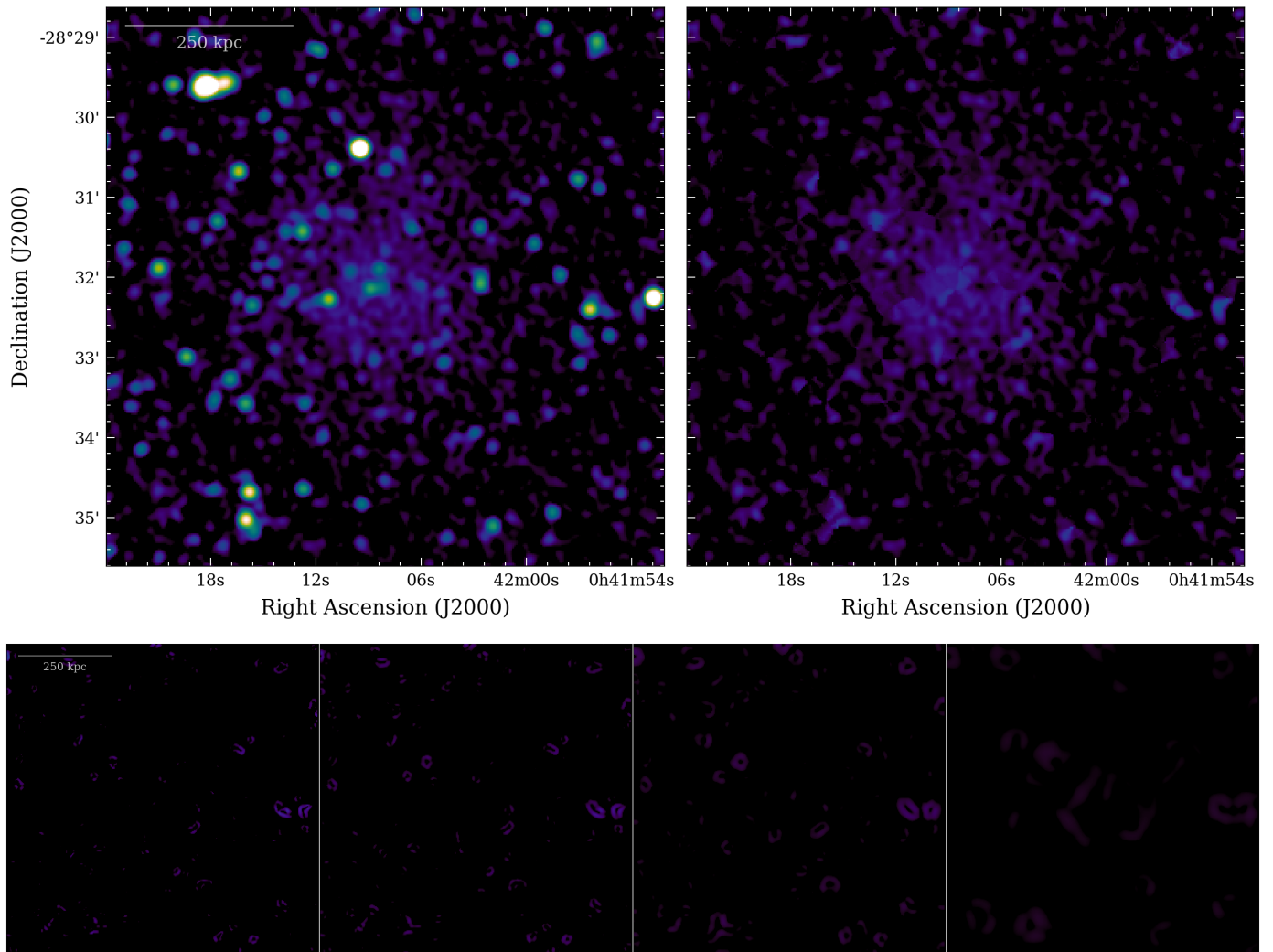


Fig. C.3. Same as Fig. 1 but for Abell 2811.

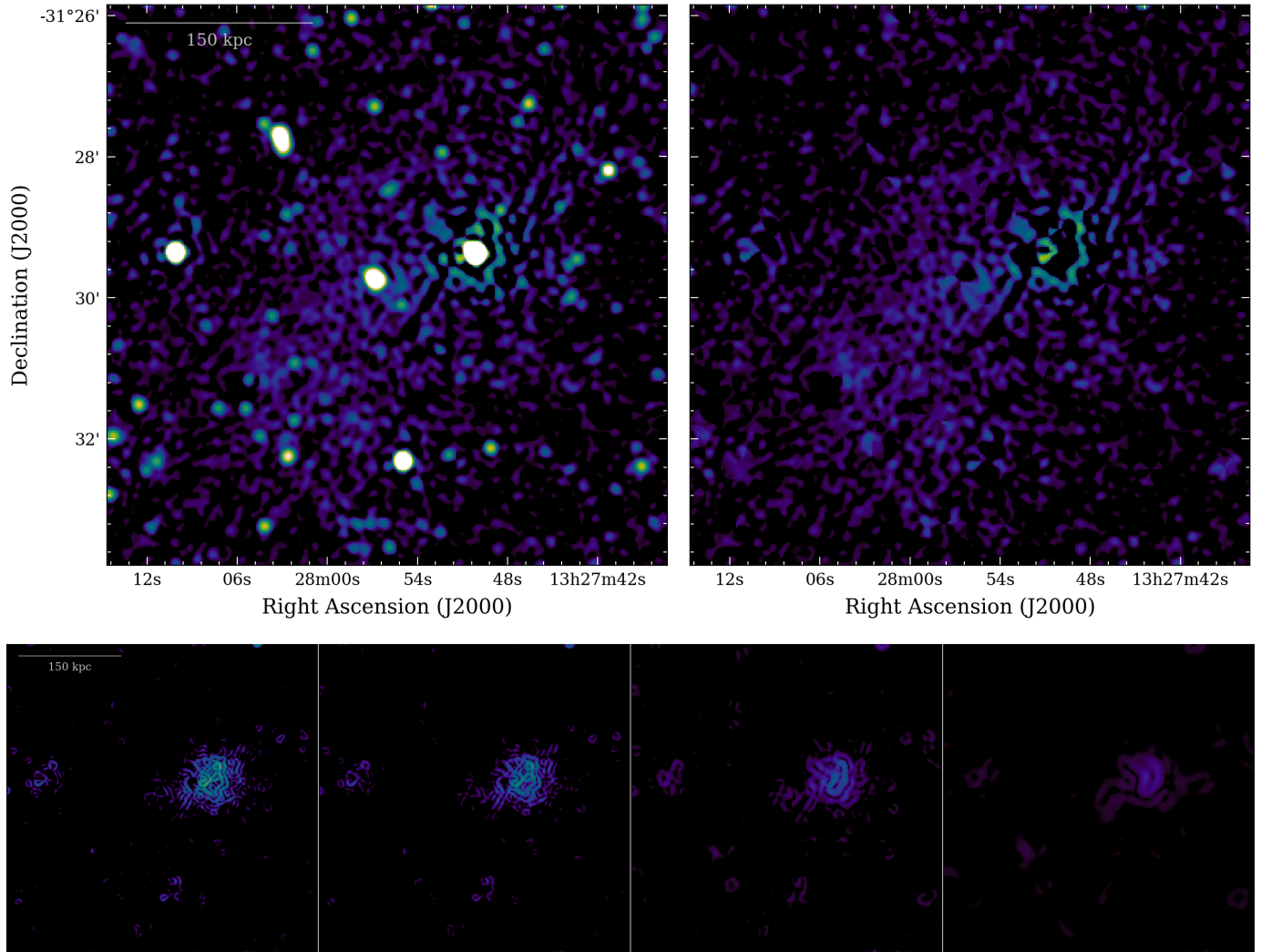


Fig. C.4. Same as Fig. 1 but for Abell 3558.

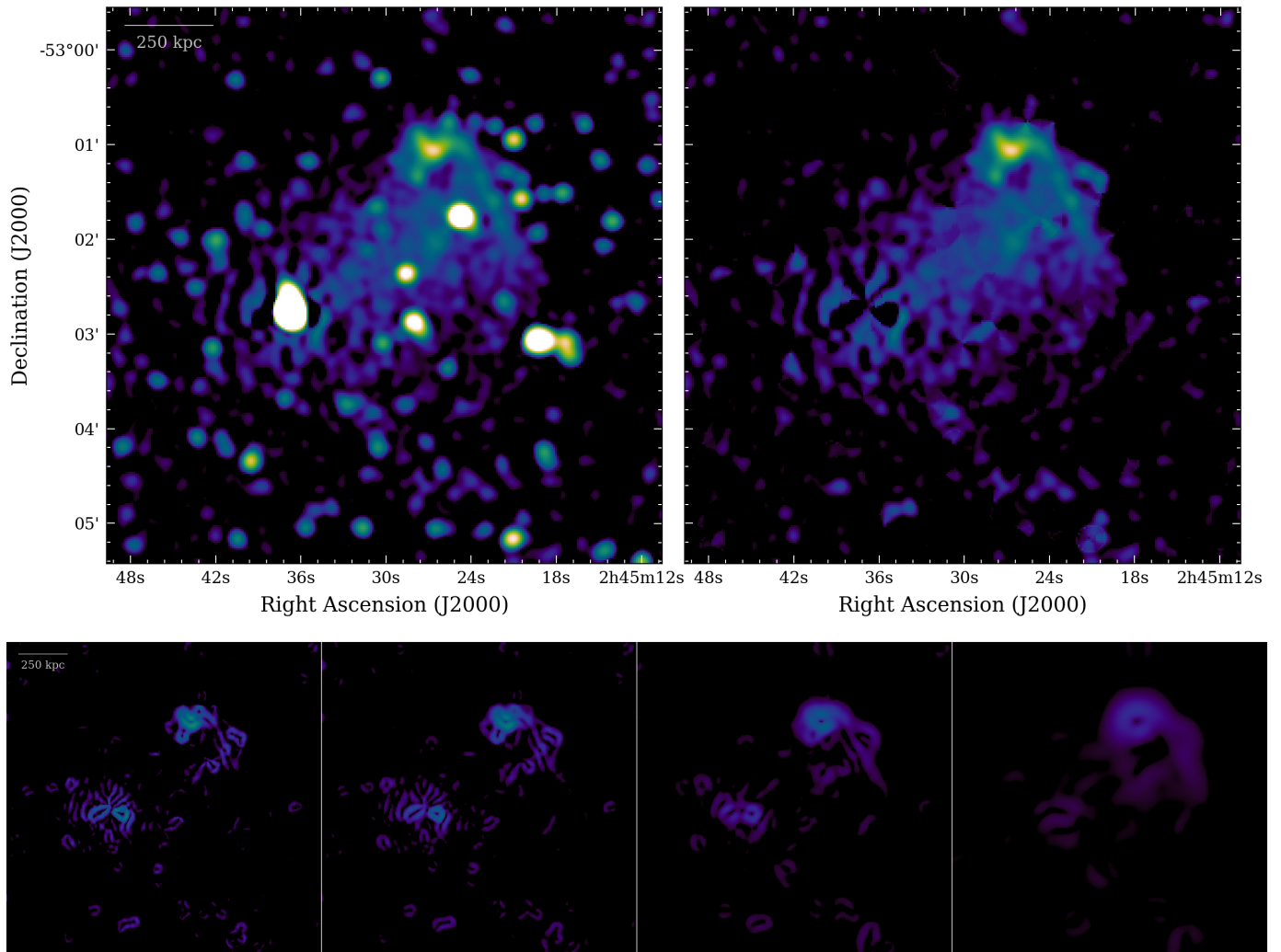


Fig. C.5. Same as Fig. 1 but for Abell S295.

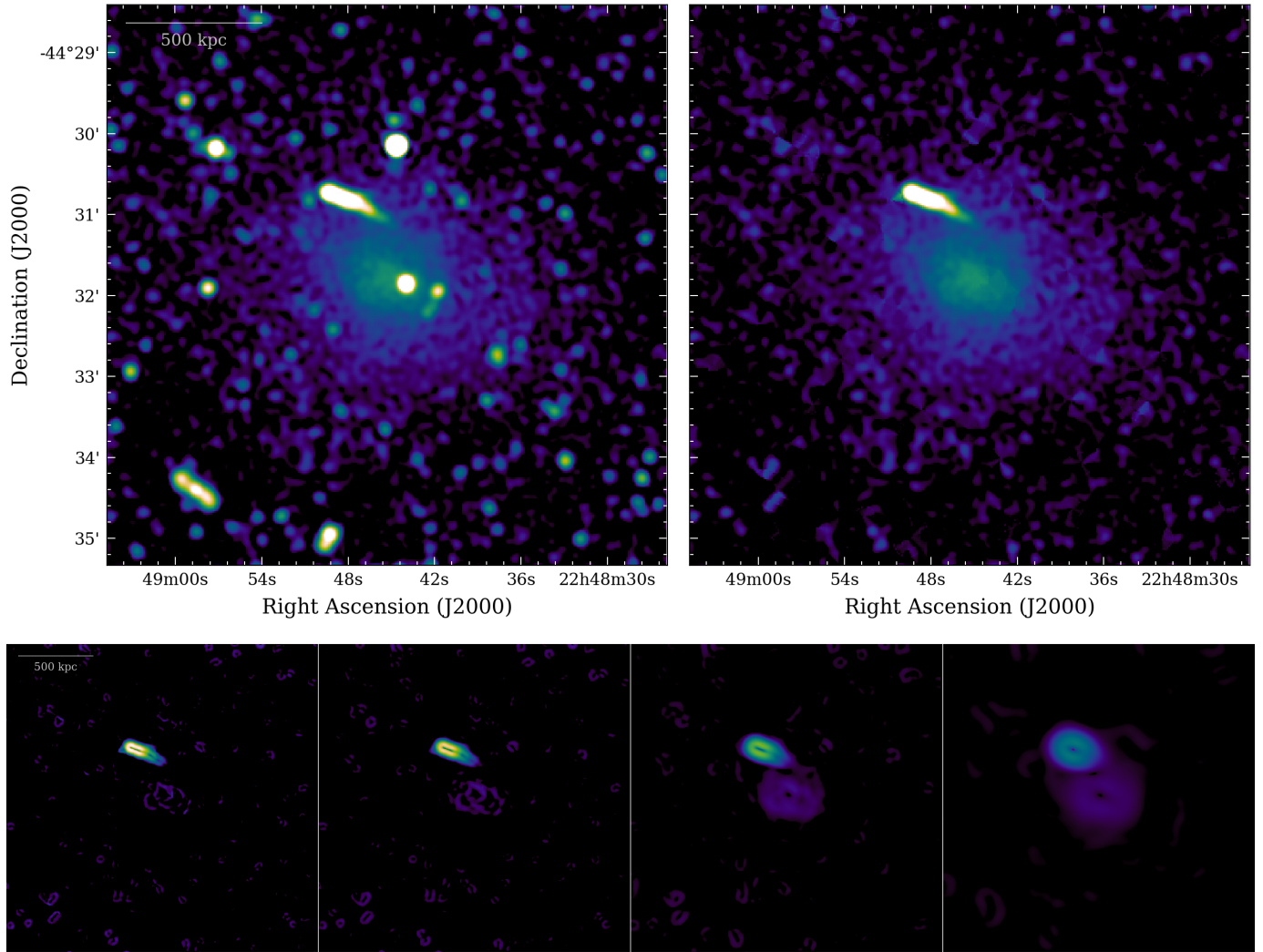


Fig. C.6. Same as Fig. 1 but for Abell S1063.

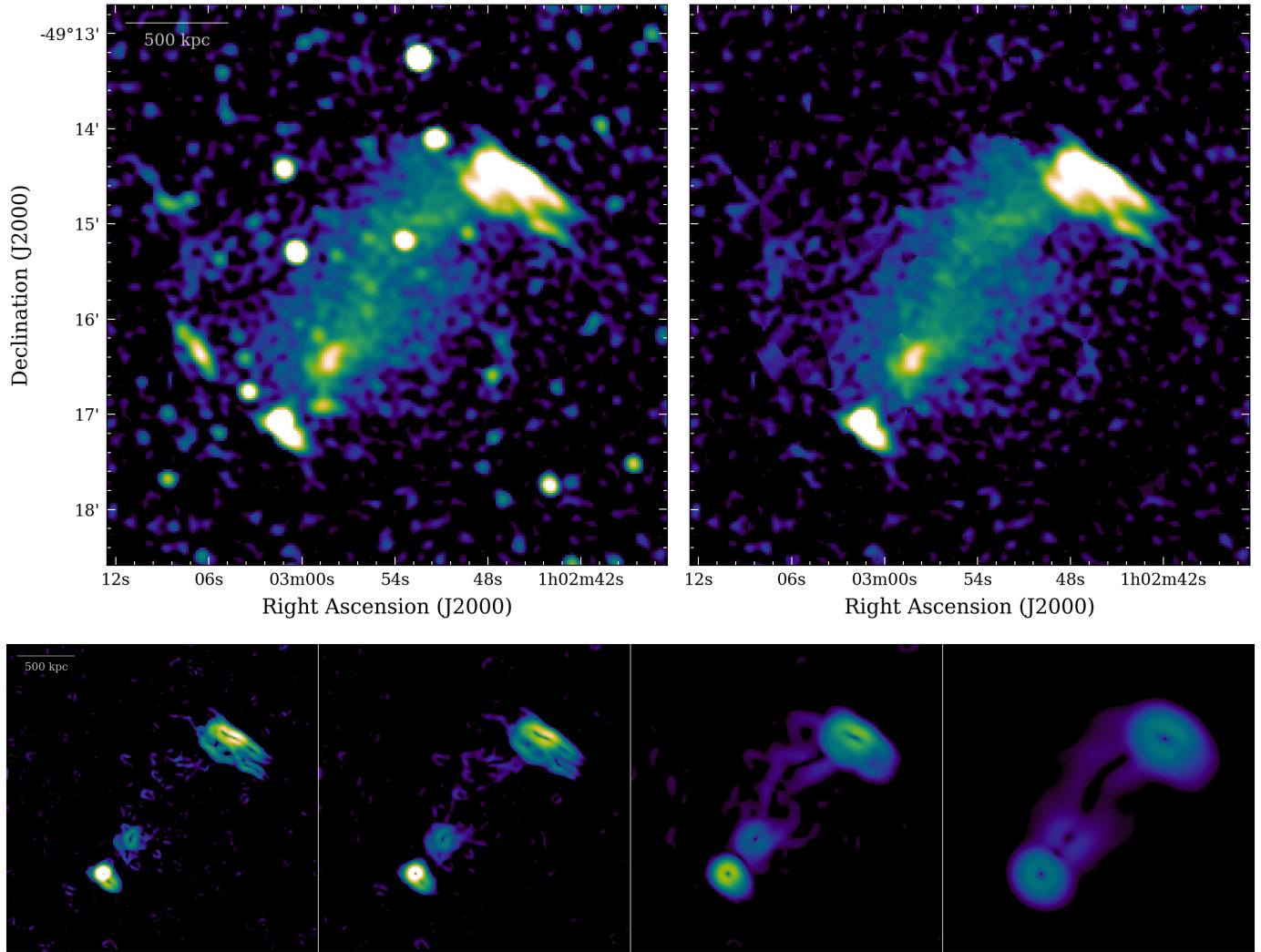


Fig. C.7. Same as Fig. 1 but for El Gordo.

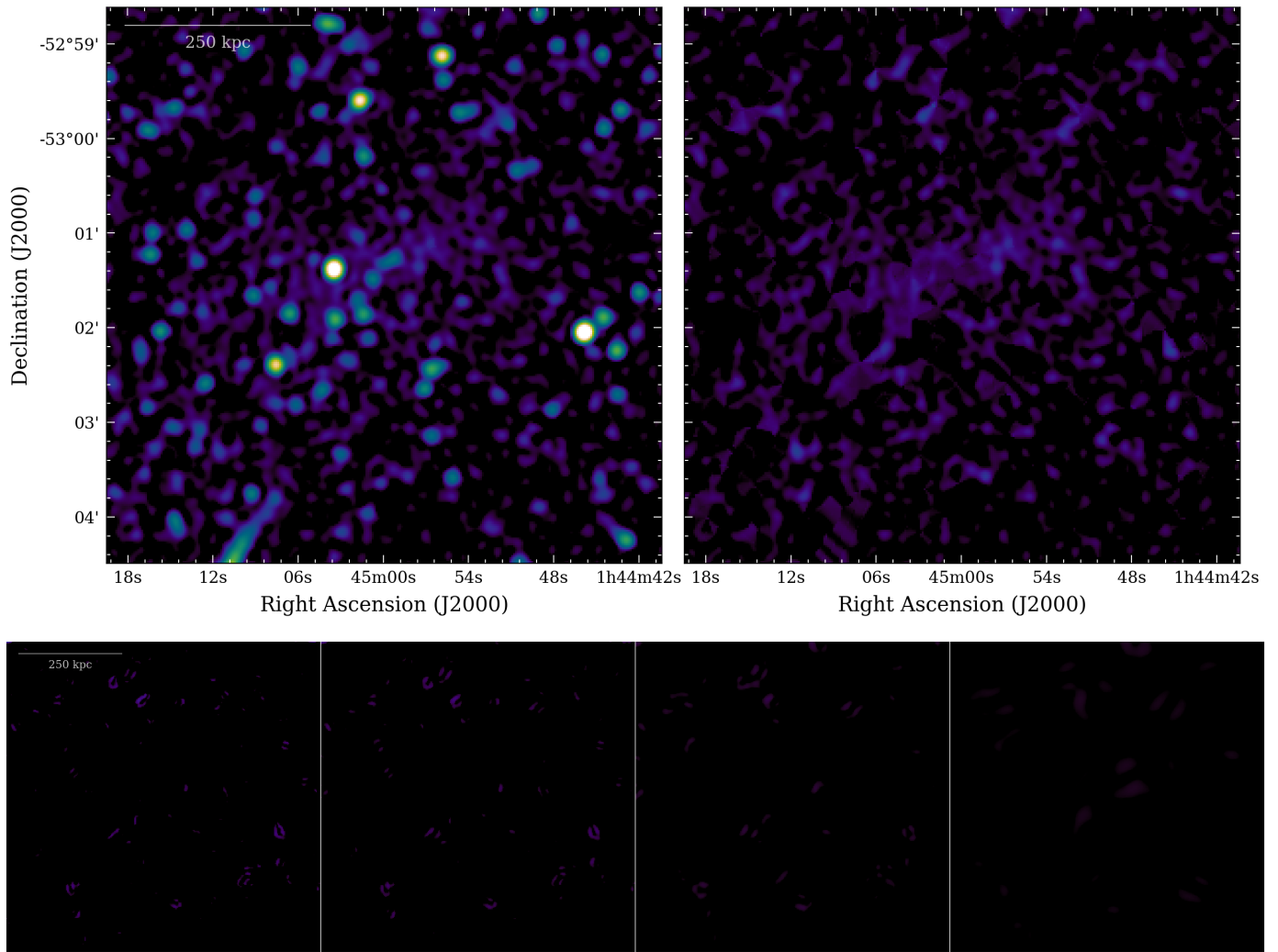


Fig. C.8. Same as Fig. 1 but for J0145.0-5300.

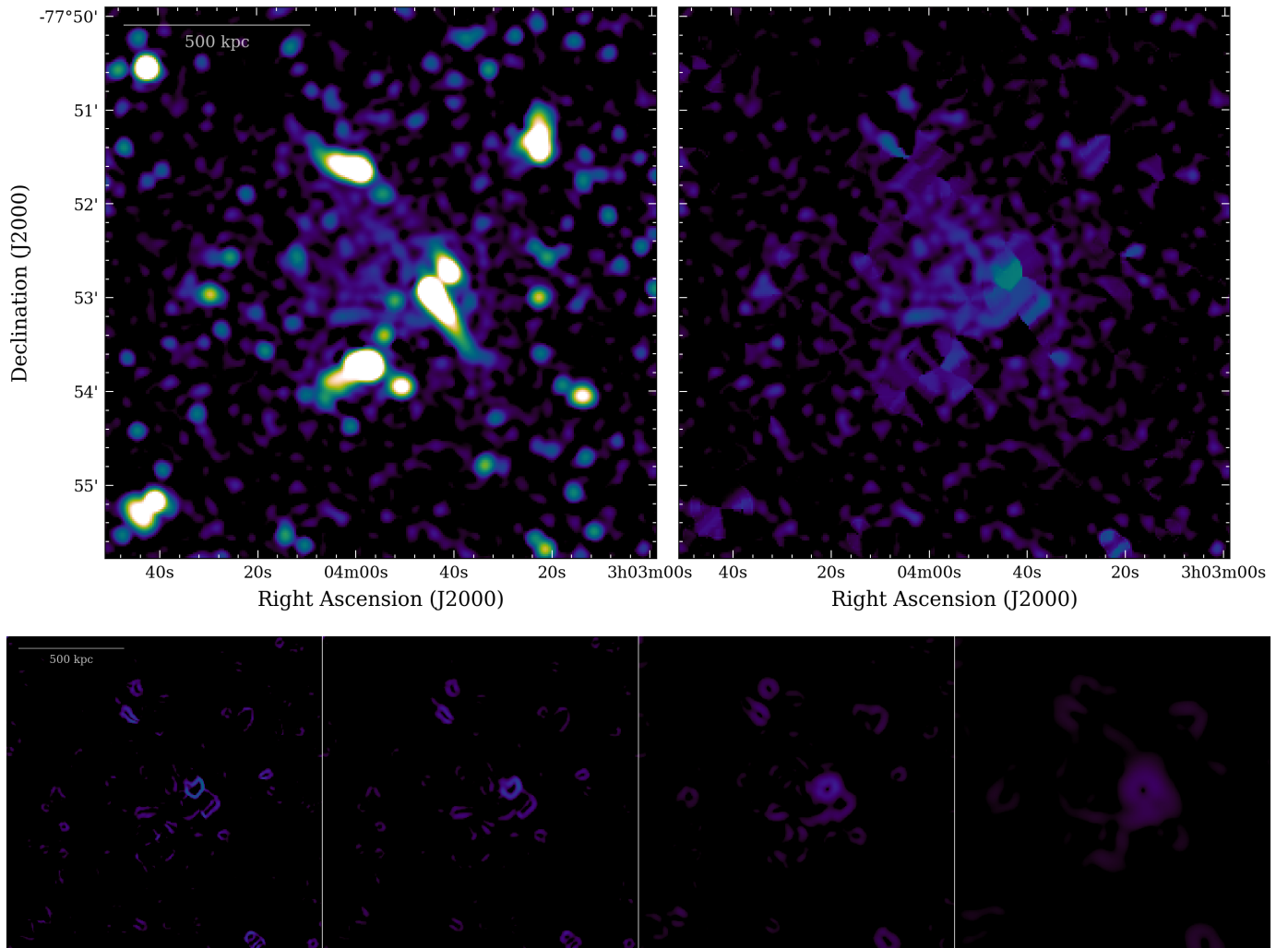


Fig. C.9. Same as Fig. 1 but for J0303.7-7752.

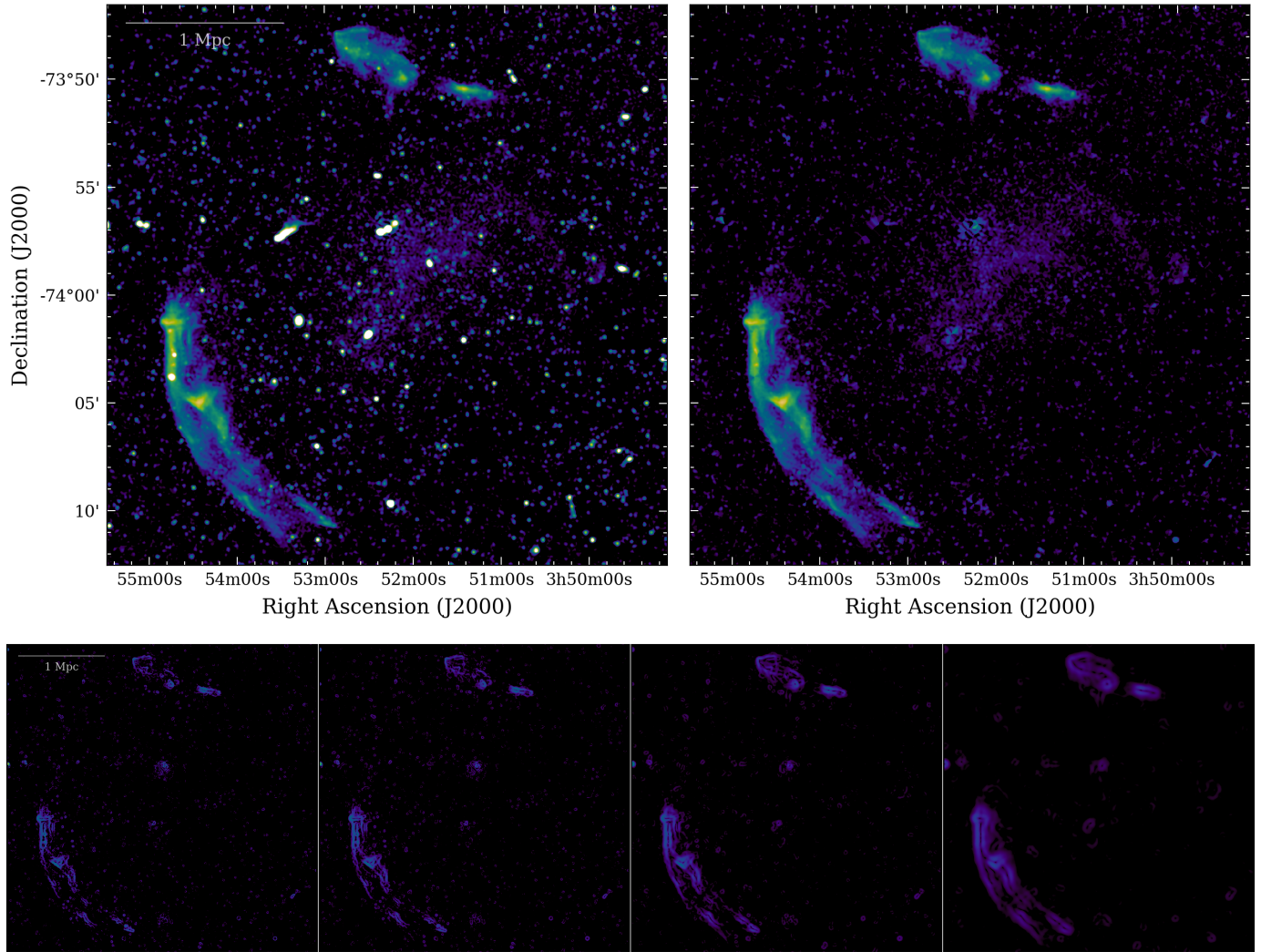


Fig. C.10. Same as Fig. 1 but for J0352.4-7401.

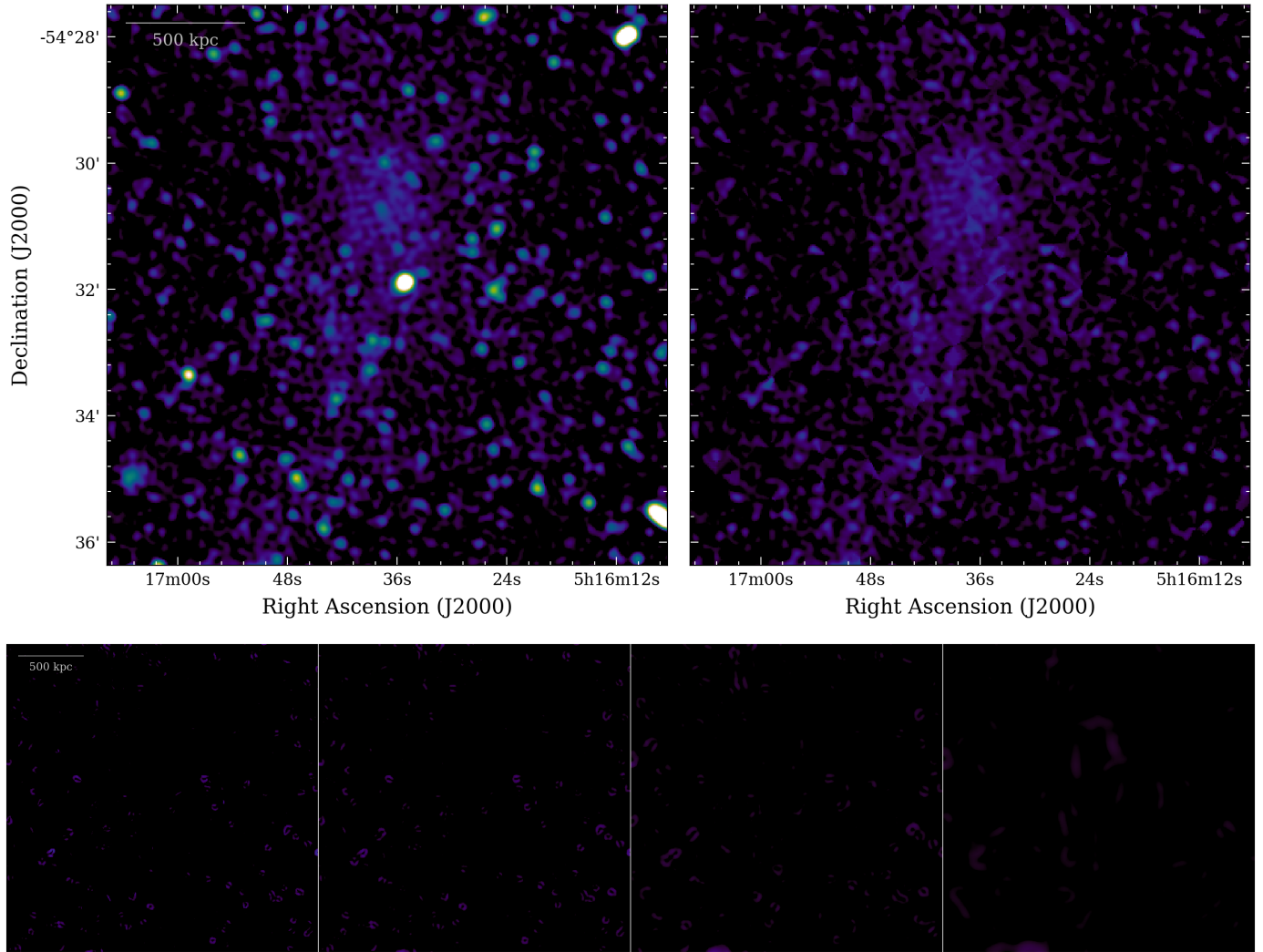


Fig. C.11. Same as Fig. 1 but for J0516.6-5430.

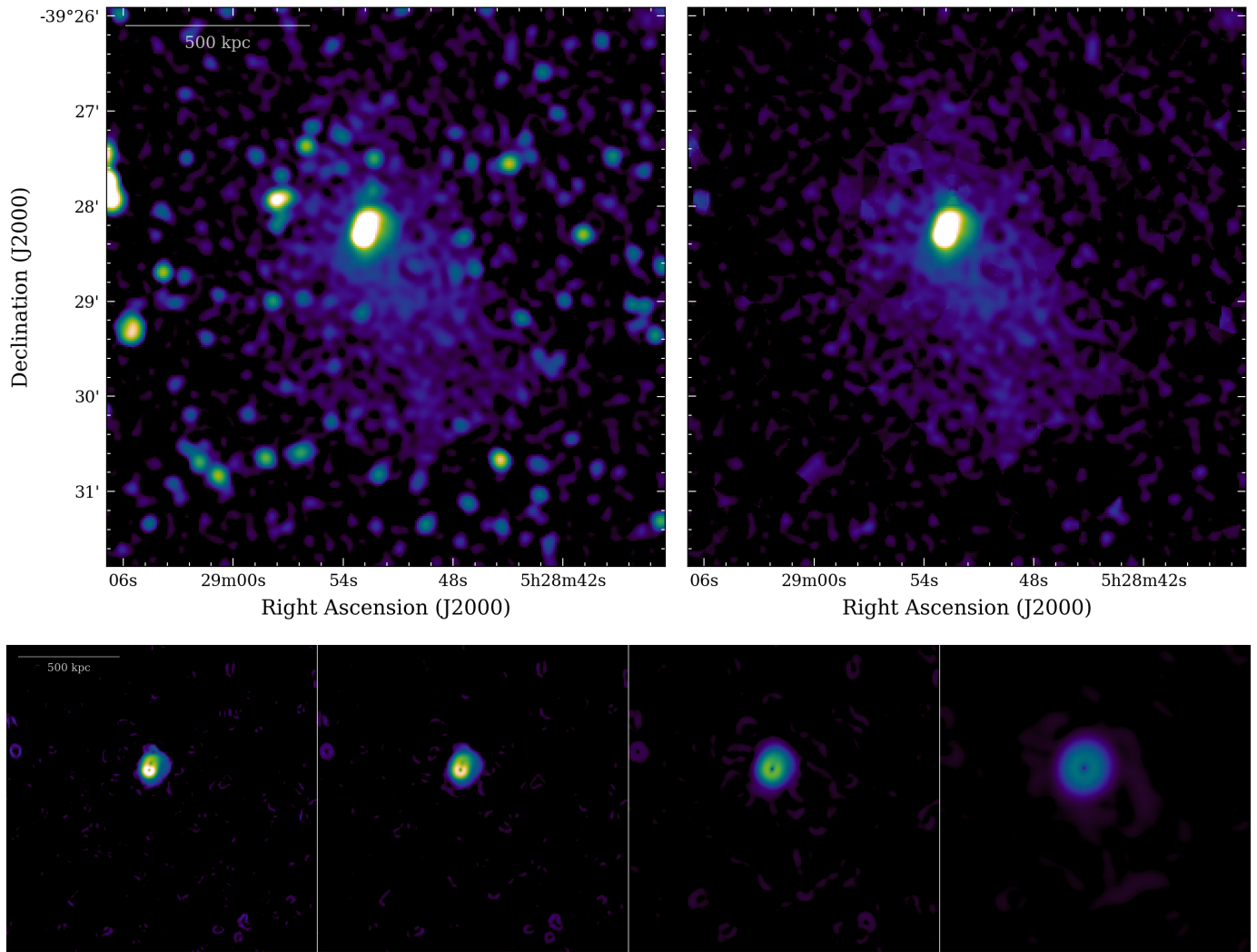


Fig. C.12. Same as Fig. 1 but for J0528.9-3927.

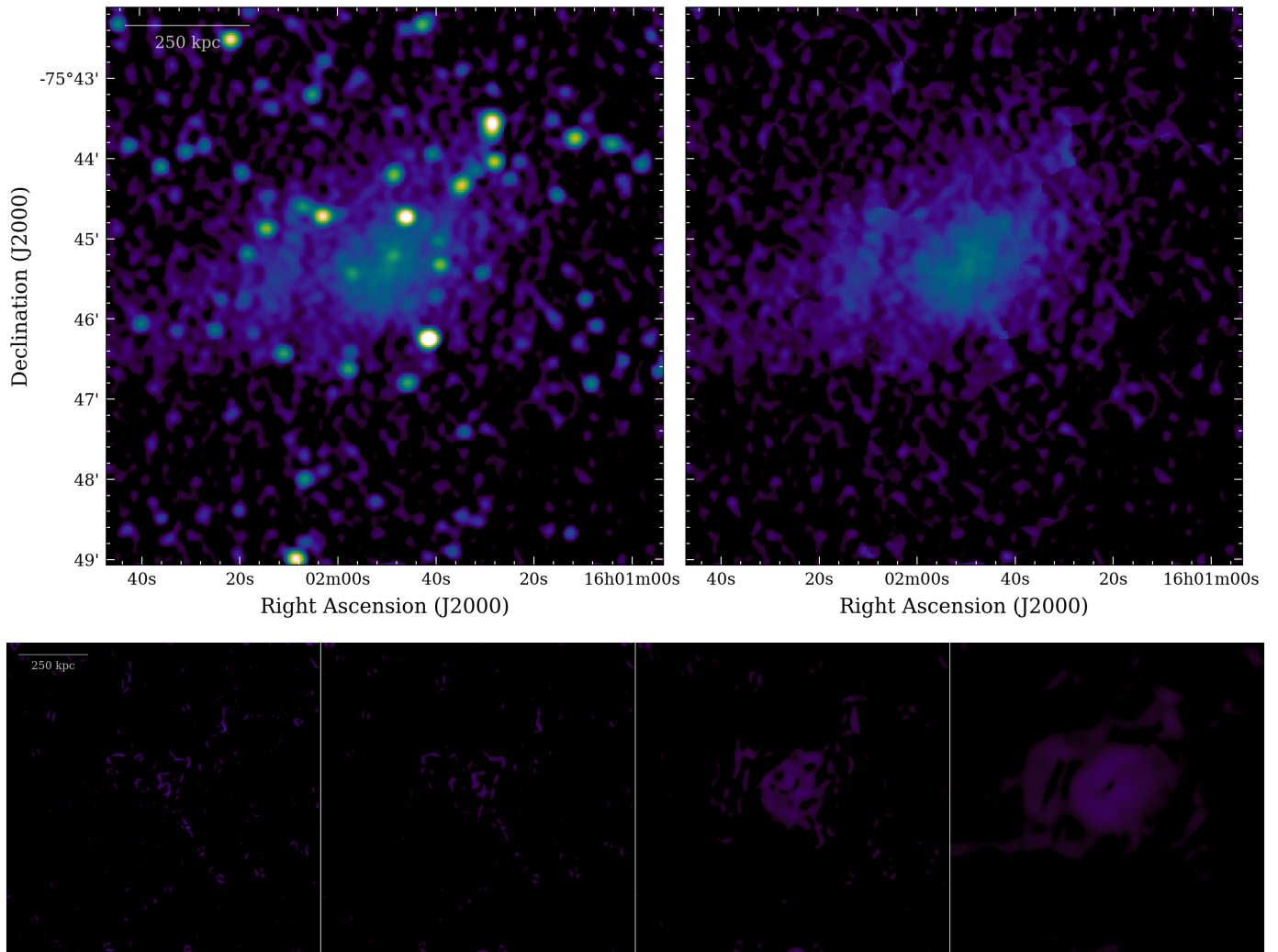


Fig. C.13. Same as Fig. 1 but for J1601.7-7544.